

OBSERVATION OF THE CASTAING INSTABILITY IN A TRAPPED ULTRACOLD BOSE GAS

by

Dorna Niroomand

B.Sc., Ferdowsi University of Mashhad, 2007

THESIS SUBMITTED IN PARTIAL FULFILLMENT
OF THE REQUIREMENTS FOR THE DEGREE OF
MASTER OF SCIENCE
IN THE
DEPARTMENT OF PHYSICS
FACULTY OF SCIENCE

© Dorna Niroomand 2013
SIMON FRASER UNIVERSITY
Spring 2013

All rights reserved.

However, in accordance with the *Copyright Act of Canada*, this work may be reproduced, without authorization, under the conditions for "Fair Dealing." Therefore, limited reproduction of this work for the purposes of private study, research, criticism, review, and news reporting is likely to be in accordance with the law, particularly if cited appropriately.

APPROVAL

Name: Dorna Niroomand
Degree: Master of Science
Title of Thesis: Observation of the Castaing instability in a trapped ultracold Bose gas
Examining Committee: Dr. J. Steven Dodge, Associate Professor (Chair)

Dr. Jeffrey M. McGuirk, Senior Supervisor
Associate Professor

Dr. Paul C. Haljan, Supervisor
Associate Professor

Dr. Malcolm P. Kennett, Supervisor
Associate Professor

Dr. Michael E. Hayden, Internal Examiner
Professor

Date Approved: April 15, 2013

Partial Copyright Licence



The author, whose copyright is declared on the title page of this work, has granted to Simon Fraser University the right to lend this thesis, project or extended essay to users of the Simon Fraser University Library, and to make partial or single copies only for such users or in response to a request from the library of any other university, or other educational institution, on its own behalf or for one of its users.

The author has further granted permission to Simon Fraser University to keep or make a digital copy for use in its circulating collection (currently available to the public at the "Institutional Repository" link of the SFU Library website (www.lib.sfu.ca) at <http://summit/sfu.ca> and, without changing the content, to translate the thesis/project or extended essays, if technically possible, to any medium or format for the purpose of preservation of the digital work.

The author has further agreed that permission for multiple copying of this work for scholarly purposes may be granted by either the author or the Dean of Graduate Studies.

It is understood that copying or publication of this work for financial gain shall not be allowed without the author's written permission.

Permission for public performance, or limited permission for private scholarly use, of any multimedia materials forming part of this work, may have been granted by the author. This information may be found on the separately catalogued multimedia material and in the signed Partial Copyright Licence.

While licensing SFU to permit the above uses, the author retains copyright in the thesis, project or extended essays, including the right to change the work for subsequent purposes, including editing and publishing the work in whole or in part, and licensing other parties, as the author may desire.

The original Partial Copyright Licence attesting to these terms, and signed by this author, may be found in the original bound copy of this work, retained in the Simon Fraser University Archive.

Simon Fraser University Library
Burnaby, British Columbia, Canada

revised Fall 2011

Abstract

Ultracold trapped atomic systems are ideal model systems to investigate physical phenomena in the quantum regime. In this work we studied instabilities in spin dynamics of a sample of nondegenerate trapped ^{87}Rb gas. This is the first experimental investigation of the so-called Castaing instability in such systems. The Castaing instability is an instability in the spin dynamics of spin-polarized systems as a result of introducing sharp spin gradients in their spin profile.

We used an optical technique via the ac Stark effect to initialize arbitrary spin profiles in a sample of evaporatively cooled nondegenerate ^{87}Rb gas. The experimental results manifest evidence for the presence of the Castaing instability in both transverse and longitudinal spin channels. The results agree reasonably well with theoretical studies and results of a numerical solution to the spin transport equation. Some imperfection in the longitudinal spin gradient due to the spin-state preparation technique makes the signature of the instability less clear in the transverse channel. We propose another preparation technique to overcome this shortcoming in future experiments.

To Sima Khosravi

*"You know how little while we have to stay,
And, once departed, may return no more..."*

- Omar Khayyam

Acknowledgments

First, I would like to thank my supervisor, Dr. Jeffrey McGuirk. This thesis would not be possible without his help and guidance. I have been fortunate to work in his group and benefit from his incredible knowledge, enthusiasm and patience. He is always supportive and willing to give advice, yet knows when to let you experience research and learn science on your own.

I am grateful for having two great physicists as committee members, Dr. Paul Haljan and Dr. Malcolm Kennett, who helped me with their wealth of knowledge throughout my studies in the last two years. Many thanks are due to Dr. Mike Hayden for his wise revision comments on this thesis.

I wish to thank my amazing friends without whom life would be a vastly boring experience. Neda Ghafoorian who has always been there for me, although on the other side of the planet. Special thanks to cheerful Zahra Mokhtari for her helpful comments on my thesis as well as her friendship. Thanks to Azadeh Akhtari, Sara Ejtemaee and Laleh Samii for their support during the tough thesis writing months, and spirited Lydia Zajiczek for great companionship in the lab.

Last and foremost, I would like to thank my family for their never ending love and support. Thank you for believing in Dorna, while she did not believe in herself.

Contents

Approval	ii
Partial Copyright Licence	iii
Abstract	iv
Dedication	v
Acknowledgments	vi
Contents	vii
List of Figures	ix
1 Introduction	1
2 Spin dynamics theory	3
2.1 A two-level system coupled to an electromagnetic field	3
2.1.1 Bloch-sphere representation and optical resonance	4
2.2 Spin dynamics and the Castaing instability	5
2.2.1 Quantum Boltzmann transport equation	7
2.2.2 Collective behavior in atomic collisions	8
2.2.3 Spin waves and the Castaing instability	8
3 Experimental design	14
3.1 Magneto-optical trap (MOT)	15
3.2 Lasers and locks	17
3.2.1 Saturated absorption spectroscopy	17
3.2.2 Phase-locked loop	19
3.3 Magnetic trap	21
3.3.1 Ioffe-Pritchard trap	21
3.3.2 From the MOT to the HIP trap	23
3.4 Evaporative cooling	26
3.5 Imaging	27

4	Spin-state preparation	31
4.1	The experimental pseudo-spin $\frac{1}{2}$ system	31
4.1.1	Differential potential	32
4.1.2	Differential Zeeman shift measurement	33
4.1.3	Cancellation of the differential shifts and uniform differential potential . .	34
4.1.4	The ac Stark effect and the light shift	36
4.2	Spin-profile initialization	37
4.2.1	Optical setup and beam shaping	37
4.2.2	Spin-state preparation	39
5	Experimental results	44
5.1	The experimental method for reconstructing spin	44
5.1.1	Longitudinal spin	45
5.1.2	Transverse spin	45
5.2	Results	47
5.2.1	Castaing instability with a longitudinal spin gradient	47
5.2.2	Castaing instability with a transverse spin gradient	51
6	Conclusion	58
	Bibliography	60

List of Figures

2.1	Bloch-sphere representation of the state vector $\vec{\psi}$ of a two-level system. The North pole corresponds to the excited state $ 2\rangle$ and the South pole corresponds to the ground state $ 1\rangle$. The azimuthal angle ϕ represents the relative phase of the superposition state.	5
2.2	Bloch-sphere representation of Rabi flopping. The black dashed vector represents the coupling field torque vector $\vec{\Omega}$, the blue vector represents the state vector ($\vec{\psi}$) and the dotted line represents the path of the oscillation of the Bloch state-vector. The coupling field is (a) in resonance with the atomic transition and (b) detuned from resonance.	6
2.3	Schematic depiction of two identical atoms colliding with each other. As the thermal de Broglie wavelength (λ_{dB}) is larger than the scattering length (a), the two scattering events, (a) forward and (b) backward scattered events are indistinguishable.	9
2.4	Schematic illustration of the spin rotation in a collision between two indistinguishable particles, using the Bloch sphere representation. The two Bloch spheres on the left represent two particles with slightly different transverse spin colliding with each other. As a result of the ISRE, the spin of each particle rotates around the total spin during the collision, which is conserved.	10
2.5	The inhomogeneous differential potential U_{diff} in the trap leads to spatially dependent precession rates for the transverse spin. The atoms in different positions in the trap are represented as Bloch spheres with spatially dependent transverse spin phase ϕ . As a result of the varying transverse spin precession rate, an inhomogeneity is created in the transverse spin profile.	10
2.6	Schematic illustration of a longitudinal spin profile containing a gradient. (a) Side view showing the longitudinal spin gradient ∇S_{\parallel} in the middle. (b) Top view showing the small transverse perturbation $\delta S_{\perp} \sin kz$	12

3.1	Trapping process in a 1D MOT. The atomic excited state is Zeeman-shifted in the magnetic field. The dashed line indicated on the diagram represents the energy of the incoming photon ($h\nu$) detuned from ground-to-excited state transition. On the right side, the incident laser frequency is closer to the transition from the ground state to the $m_f = -1$ excited state, as the $m_f = -1$ state is shifted down due to the Zeeman shift. Therefore the transition with $\Delta m = -1$ is closer to be resonant with the illuminating laser and the atoms on that side scatter σ^- photons at a higher rate than the σ^+ photons. Choosing the right polarization of the incident beams leads to driving the atoms towards the center of the trap.	16
3.2	MOT setup. A pair of electromagnetic coils in anti-Helmholtz configuration produces a quadrupole magnetic field. Counter-propagating laser beams with opposite polarization are used to confine the atoms in three dimensions.	16
3.3	Schematic representation of the hyperfine structure of the D_2 transition ($5^2S_{1/2} \rightarrow 5^2P_{3/2}$) of ^{87}Rb in zero magnetic field. The cooling transition ($F = 2 \rightarrow F' = 3$) and repumper transition ($F = 1 \rightarrow F' = 2$) are indicated on the diagram.	18
3.4	Schematic of our SAS setup. Counter-propagating pump and probe beams from the same laser separated by a beam splitter pass through a Rb vapor cell. The absorption profile of the probe beam is compared to a reference beam. An error signal is sent back to the laser controller. Arrows show the beam directions.	19
3.5	(a) Absorption spectral lines of ^{87}Rb for the $F = 2 \rightarrow F' = 1', 2'$ and $3'$ and cross-over transitions. (b) Error signal for the $F = 2 \rightarrow F' = 1', 2'$ and $3'$ and cross-over transitions. Image courtesy of R. Thomas.	20
3.6	Schematic of our PLL setup. The laser beam is mixed with another laser beam with a known fixed frequency. Some arrows indicate beam direction. The resulting beatnote is collected on a photodiode and mixed with a local oscillator (LO) signal. The phase-frequency detector compares this signal to a reference, and the error signal is sent back to the laser controller to modify the laser frequency. The locked laser's linewidth is well below the transition linewidth of 6 MHz.	20
3.7	Hybrid Ioffe-Pritchard trap. Opposite currents pass through the pinch and bias coils. The bias coils are in a Helmholtz configuration, producing a uniform magnetic field in the center of the trap.	22
3.8	HIP trap end-on view. This configuration of permanent magnets produces a radial quadrupole field and no field along the axial direction.	23
3.9	(a) Axial and (b) radial trap frequency measurement data. Using an extra electromagnetic coil placed near the trap, axial or radial oscillations are induced in the trap. The position of the center of the trapped atomic cloud is measured as a function of time to extract the trap frequencies.	24
3.10	Zeeman-shifted ^{87}Rb hyperfine splitting in a magnetic field. It is evident that in low magnetic fields, the energy of the $ 1, -1\rangle$ state increases with magnetic field.	25

3.11	Schematic representation of the Zeeman-shifted ground ($5S_{1/2}$) and excited ($5P_{3/2}$) states of ^{87}Rb in low magnetic fields. The ARP ($ 1, -1\rangle \rightarrow 2, -2\rangle$) and imaging ($ 2, -2\rangle \rightarrow 3', -3\rangle$) transitions are shown on the diagram as solid arrows. The dashed arrows indicate the transitions for the $m_f = 0$ levels.	28
4.1	Zeeman-shifted ground state hyperfine levels of ^{87}Rb in low magnetic field. The pseudo-spin $\frac{1}{2}$ system consists of the two trapped states ($ 1, -1\rangle$ and $ 2, 1\rangle$) coupled via a two-photon transition. The coupling fields are detuned from the intermediate $ 2, 0\rangle$ state to avoid real transitions.	32
4.2	Schematic representation of the cancellation of the differential mean-field and Zeeman shifts. The mean-field differential potential is a Gaussian, while the Zeeman shift approximately scales as z^2 . The total differential potential is roughly uniform across the atomic cloud.	33
4.3	Differential Zeeman shift $\frac{1}{h} [E_{12} - E_{\text{hf}}(B = 0)]$, for the $ 1, -1\rangle \rightarrow 2, 1\rangle$ transition in low magnetic fields. The red curve is a fit to the quadratic approximation of the Breit-Rabi equation for scale parameter a in $B = B_{\text{Pinch}} - aV_{\text{Bias}}$	35
4.4	Uniform differential potential is achieved by cancellation of the differential Zeeman shift and the collisional mean-field shift. We measure differential energy shifts by means of Ramsey spectroscopy (Section 5.1.2). We obtain spatially resolved data by dividing the atomic cloud axially into 23 bins across the cloud and radially averaging over each bin.	36
4.5	A step optical potential is produced by masking the off-resonant laser beam (schematic representation).	38
4.6	Optical setup used in producing the step optical potential presented in Fig. 4.7. The collimated beam from the laser is expanded axially using a pair of cylindrical lenses. The dark mask is imaged on the atomic cloud by a single spherical lens.	38
4.7	Step optical potential (\bullet) with $dU_{\text{diff}}/dz \simeq h \times 500 \text{ Hz/mm}$ created by illuminating the atomic cloud with a masked laser beam. The black data points (\blacksquare) shows the uniform differential potential with no laser field applied. U_{diff} is measured by means of Ramsey spectroscopy.	39
4.8	The longitudinal spin gradient initialization sequence. Turning on the Stark laser when the system is in a superposition of the states $ 1\rangle$ and $ 2\rangle$ (<i>i.e.</i> after the first $\pi/2$ pulse) imprints a phase profile onto the transverse spin component. A second $\pi/2$ pulse maps the transverse spin into the longitudinal component.	40
4.9	(a) Population distribution between states $ 1\rangle$ (\bullet) and $ 2\rangle$ (\blacksquare) along the axial extent of the atomic cloud, demonstrating the presence of a longitudinal spin gradient. The longitudinal spin profile is obtained by directly measuring the populations N_1 and N_2 of the atoms in the two states immediately after the spin-profile initialization. (b) The longitudinal spin, $S_{\parallel} = \frac{1}{2} (N_2 - N_1) / (N_1 + N_2)$. The gradient length scale implied by this data is $l_{\nabla S_{\parallel}} \simeq 1.1 w_z$, where w_z is the Gaussian half-width of the atomic distribution in the axial dimension.	41

4.10	(a) The Bloch sphere representation of an atom on the bright (perturbed) side of the sample. The state vector $\vec{\psi}$ (blue arrow) undergoes a small precession around the field's torque vector $\vec{\Omega}$ (dashed arrow) which is far detuned from resonance. (b) The Bloch sphere representation of an atom on the dark (unperturbed) side of the sample. The state vector $\vec{\psi}$ oscillates between the two states, precessing around the field's torque vector $\vec{\Omega}$ which is on resonance.	43
5.1	Population of atoms in the two states, $ 1\rangle$ (●) and $ 2\rangle$ (■). The population in each state is measured in separate experimental shots. As described earlier the cloud is divided axially into 23 bins for spatial resolution; here each data point corresponds to one bin. These data are used to reconstruct the longitudinal spin component. . .	45
5.2	Ramsey spectroscopy sequence.	46
5.3	Schematic representation of Ramsey oscillations in the Bloch sphere representation, showing two $\pi/2$ pulses detuned by $\delta = \omega - \omega_0$ and separated by an evolution time T . The blue dashed arrow indicates the initial state. (a) When $\delta T = 0$ the two-pulse sequence is equivalent to a π pulse. (b) When $\delta T = \frac{\pi}{2}$ the second $\pi/2$ pulse does not transfer the atoms into state $ 2\rangle$ as the state vector is along the field's torque vector (U -axis). (c) When $\delta T = \pi$ the second $\pi/2$ transfers the atoms back into the initial state $ 1\rangle$	48
5.4	Typical Ramsey oscillation data. The curve represents a sine wave fit to the data. . .	48
5.5	Ramsey oscillations for a bin at $z = 250 \mu\text{m}$ from the center of the atomic cloud. The initial fringe amplitude is small, but is followed by a rapid rise. The solid line represents a fit to a damped sine wave to guide the eye.	50
5.6	Ramsey oscillations in the middle of the atomic cloud. There is a large initial transverse spin component due to the spin-state preparation technique. The solid line represents a fit to a damped sine wave to guide the eye.	50
5.7	A sine wave with a fixed frequency but a time varying amplitude and phase is fit to the data points in a window with a width that encompasses more than one oscillation. This window is moved in time through the data set to extract the time evolution of the amplitude and phase of the Ramsey oscillations. The solid line is a fit of a damped sine wave to guide the eye.	51
5.8	Time evolution of the magnitude of the transverse spin in a cloud initialized with a longitudinal spin gradient. These results are extracted from raw Ramsey oscillation data by fitting a sine wave with a time varying amplitude and phase to Ramsey oscillations. The extracted amplitude of the Ramsey oscillations is normalized with the mean value of the Ramsey oscillations in each bin. The black curve (●) indicates data acquired at $z = 250 \mu\text{m}$ from the center of the atomic cloud (Fig. 5.5) where the initial condition corresponds to a nearly pure longitudinal spin state with a small initial transverse spin component. After a short delay a rapid rise in the magnitude of the transverse spin is observed. The red curve (■) corresponds to the center of the cloud where a large initial transverse spin component is present.	52

5.9	Time evolution of the transverse spin phase in a system initialized with a longitudinal spin gradient. The red, blue and black curves show the right, middle and left sides of the sample respectively. At $T = 280$ ms a sudden inversion in the orientation of the transverse spin is observed on the edges of the cloud.	53
5.10	Ramsey spectroscopy data (a) in the middle and (b) at $z = 250 \mu\text{m}$ from the center of the atomic cloud, for a system initialized with a gradient in the transverse spin profile. A damped sine wave is fit to the experimental data points to guide the eye. The phase is then measured using the running-window fit described in Section 5.2.1.	54
5.11	Time evolution of the transverse spin phase in a cloud initialized with a sharp gradient in the transverse spin profile measured using the running-window fit described in Section 5.2.1. The red, blue and black curves show the right, middle and left sides of the sample respectively. Initially there is a π difference in the transverse spin phase across the cloud. Very little happens for the first 150 ms followed by a sudden inversion of the transverse spin phase on opposite sides of the cloud. The time defined as the spin inversion time is indicated on the plot with a dashed line. This inversion time corresponds to the time when the initial spin orientation angle passes through zero as it inverts to an opposite value. The spin inversion rate inferred from these data is 5.5 ± 0.3 Hz.	56
5.12	Experimental results along with numerical solution of the spin transport equation showing the spin inversion rate as a function of the magnitude of the initial spin difference. The black curve shows the simulation results for an initial transverse spin profile containing a sharp gradient with a length scale on the order of w_z . The red curve shows the solution for similar initial conditions with a linear differential potential of the same magnitude but no sharp gradient. It is evident that the presence of the gradient leads to increased spin inversion rates. The experimental results agree with the simulation results.	57

Chapter 1

Introduction

The experimental realization of Bose-Einstein condensation in 1995 [1, 2] led to the Nobel prize for E. A. Cornell, C. E. Wieman and W. Ketterle in 2001. Bose-Einstein condensation (BEC) is a phase transition of an ensemble of bosons below a critical temperature T_c , in which a macroscopic population of particles occupies a single quantum state. This phase transition was predicted by Bose and Einstein in the early 1900s but it took experimental physicists nearly a century to condense the first BEC of a trapped Alkali-metal gas.

Aside from this huge scientific achievement, the experimental efforts to reach condensation in Alkali-metal atomic gases turned out to be a robust foundation for a whole new field of research, which provides physicists with a number of novel advantages. In trapped ultracold atomic gas systems the experimental parameters are highly controllable. These systems are also easy to manipulate and image. The aforementioned properties make these systems ideal model systems to investigate physical problems in the quantum regime.

While most studies in this field are involved with BECs such as quantum magnetism in spinor BECs [3], quantum information [4] and precision measurements [5] to name a few, observation of unexpected collective behavior in noncondensed spinor gases opened up a somewhat different playground for atomic physicists [6]. Using an analogy between a two-component gas and a spin- $\frac{1}{2}$ system, the observed collective behavior was explained as pseudo-spin oscillations (spin waves) due to a spin rotation effect [7] occurring during collisions between indistinguishable particles [8, 9, 10, 11]. Although these systems are nondegenerate, quantum scattering effects can occur as a result of indistinguishability and symmetrization properties of wave functions [12], given that the thermal de Broglie wavelength (λ_{dB}) of the particles is comparable to the scattering length between them.

Theoretical studies by A. Kuklov and A. E. Meyerovich proposed that this analogy between a two-component gas and a spin- $\frac{1}{2}$ system is more fundamental [13]. They predicted the presence of other types of dynamics in these systems such as the Castaing instability, the experimental study of which is the subject matter of this thesis. The Castaing instability is a phenomenon occurring in the spin dynamics of a system in the presence of a nonequilibrium spin gradient, which results in spontaneous generation of spin waves in the system. The work presented in this thesis is the first experimental study investigating the presence of the Castaing instability in a trapped ultracold atomic gas system. In the Castaing experiments in spin polarized ^3He - ^4He samples the observed signal was averaged over the whole sample. The advantages trapped atomic systems provide, specifically the spatial resolution, allows us to investigate the localized behavior of the instability.

The organization of this thesis is as follows. Chapter 2 is devoted to a mathematical description of a two-level (pseudo-spin $\frac{1}{2}$) system, followed by a theoretical discussion of spin dynamics predicting the potential for the Castaing instability to arise in trapped ultracold atomic systems. Chapter 3 presents the experimental apparatus as well as the procedure used to create and detect an ultracold atomic sample. Chapter 4 focuses on the experimental pseudo-spin system and the spin-state preparation techniques. The spin profile created for investigating the Castaing instability is then presented and characterized at the end of that chapter. Finally, experimental results revealing evidence for the presence of the Castaing instability are presented in Chapter 5.

Chapter 2

Spin dynamics theory

In this chapter a brief description of the spin dynamics theory in ultracold noncondensed atomic samples is given. I will start by describing a two-level system coupled to an electromagnetic field, which is analogous to a spin- $\frac{1}{2}$ system. I will then present the spin transport equation and discuss the situation relevant to the Castaing instability.

2.1 A two-level system coupled to an electromagnetic field

A two-level system is conceptually the same physical object as a spin- $\frac{1}{2}$ doublet. This analogy can be extended to interactions with electromagnetic fields. The Hamiltonian of a two-level system coupled to an electromagnetic field is

$$H = \begin{pmatrix} \frac{\hbar\omega_0}{2} & \Omega_R e^{\frac{i\omega t}{2}} \\ \Omega_R e^{-\frac{i\omega t}{2}} & -\frac{\hbar\omega_0}{2} \end{pmatrix}, \quad (2.1)$$

where ω is the frequency of the coupling field, ω_0 is the atomic resonance frequency and Ω_R is the Rabi frequency, which characterizes the coupling strength between the field and the atoms.

Solving the time-dependent Schrödinger's equation gives the probability of finding the atoms in the ground or excited state denoted by $|1\rangle$ and $|2\rangle$ respectively as a function of time. Starting with the system in the ground state ($P_1(0) = 1$ and $P_2(0) = 0$), the probability of finding the system in

the excited state at time t is [14]

$$P_2(t) = \left(\frac{\Omega_R}{\Omega'_R} \right)^2 \sin^2 \left(\frac{\Omega'_R t}{2} \right). \quad (2.2)$$

The effective Rabi frequency, Ω'_R , is

$$\Omega'_R = \sqrt{\Omega_R^2 + \delta^2}, \quad (2.3)$$

where $\delta = \omega - \omega_0$ is the detuning of the coupling field from the atomic transition.

This population oscillation between the two states is referred to as Rabi flopping. The energy splitting between the two energy levels in a two-component system can be measured using the detuning dependence of Rabi flopping. However, as the atomic energy splitting is altered by a radiation field due to the ac Stark effect, the measured effective Rabi frequency depends on the power of the coupling field. This power dependence limits the accuracy with which the energy splitting can be measured.

2.1.1 Bloch-sphere representation and optical resonance

The Bloch-sphere representation is a pictorial method for representing the Rabi problem, in which the system is described as a state vector $\vec{\psi}$ (Bloch vector) in a three-dimensional space (U, V, W) (Fig. 2.1). The vertical axis (W) represents S_{\parallel} , the longitudinal spin component. The horizontal plane ($U - V$) corresponds to S_{\perp} , the transverse spin component, where the azimuthal angle ϕ indicates the relative superposition phase.

The interaction between a two-level system and an electromagnetic coupling field can be considered as a torque vector with components $(\Omega_R, 0, \delta)$ acting on the state vector of the system. In order to reach this simplification, a transformation to a frame rotating at the coupling field's frequency ω and implementation of the rotating-wave approximation is needed [15]. The motion of the Bloch vector described by

$$\frac{d\vec{\psi}}{dt} = \vec{\Omega} \times \vec{\psi} \quad (2.4)$$

is confined to the surface of a sphere (Fig. 2.1).

When the electromagnetic coupling field is close to resonance, the field's torque vector lies close to the equator. As a result the Bloch vector ($\vec{\psi}$) that is precessing around the field's torque vector

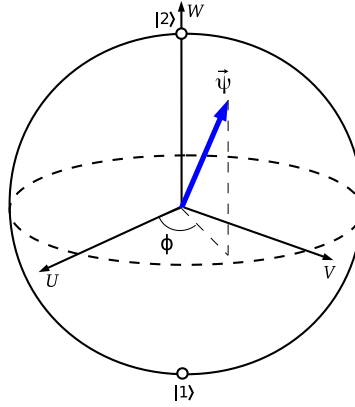


Figure 2.1: Bloch-sphere representation of the state vector $\vec{\psi}$ of a two-level system. The North pole corresponds to the excited state $|2\rangle$ and the South pole corresponds to the ground state $|1\rangle$. The azimuthal angle ϕ represents the relative phase of the superposition state.

$(\vec{\Omega})$ oscillates between the two pure states $|1\rangle$ and $|2\rangle$ (Fig. 2.2a). When the field is detuned from the atomic resonance, the field's torque vector approaches one of the poles (depending on the sign of the detuning). In this case the Bloch vector undergoes rapid precession with a small radius about the torque vector, nearly staying in its initial state (Fig. 2.2b).

2.2 Spin dynamics and the Castaing instability

The thermal de Broglie wavelength (λ_{dB}) of particles with mass m at temperature T is given by

$$\lambda_{dB} = \sqrt{\frac{2\pi\hbar^2}{mk_B T}}, \quad (2.5)$$

where \hbar is the reduced Planck constant and k_B is the Boltzmann constant. When this wavelength is small compared to other typical length scales in a system, quantum effects can be neglected [16]. For example for liquid ^4He at $T = 4$ K the thermal de Broglie wavelength is $\lambda_{dB} \approx 0.4$ nm, which is larger than interatomic distances (typically $d \approx 0.27$ nm). Thus we expect liquid ^4He typically to behave quantum mechanically.

Although in noncondensed ultracold atomic gas samples the system is nondegenerate, the thermal de Broglie wavelength λ_{dB} is typically comparable to the scattering length. For ^{87}Rb atoms at $T = 600$ nK, the thermal de Broglie wavelength is $\lambda_{dB} \approx 240$ nm, which is much larger than

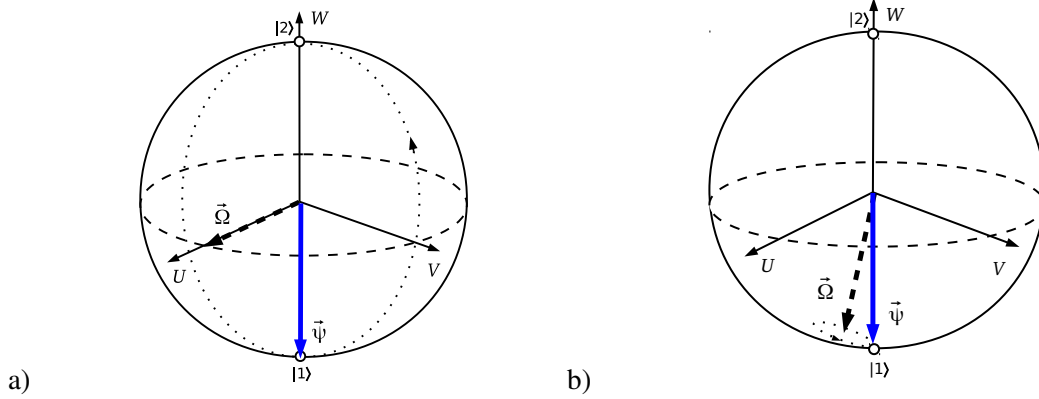


Figure 2.2: Bloch-sphere representation of Rabi flopping. The black dashed vector represents the coupling field torque vector $\vec{\Omega}$, the blue vector represents the state vector ($\vec{\psi}$) and the dotted line represents the path of the oscillation of the Bloch state-vector. The coupling field is (a) in resonance with the atomic transition and (b) detuned from resonance.

the s-wave scattering length, $a = 5.3$ nm. As a result, quantum properties of particles such as indistinguishability and symmetrization properties of wave functions dominate the dynamics, and thus collisions occur in a quantum regime, leading to a number of interesting quantum phenomena. One such phenomenon is the Castaing instability in the spin dynamics of spin-polarized systems, the experimental study of which is the subject matter of this thesis. In this section I will present a short background description of spin dynamics in noncondensed ultracold atomic systems, followed by a discussion of the predictions of the Castaing instability.

Collective behavior in noncondensed two-component trapped atomic gases was first observed in 2002 [6], when the two components (spin states) of a trapped ^{87}Rb gas sample became segregated spatially, a situation that could not be described by thermal energy considerations. Theoretical descriptions of this experiment made an analogy between a two-component gas and a spin-polarized gas. This phenomenon was explained as manifestation of pseudo-spin oscillations (spin waves) arising from a spin rotation (the identical spin rotation effect [7] or Leggett-Rice rotation [17]), which occurs in collisions between indistinguishable particles in the quantum regime (see Section 2.2.2).

A. Kuklov and A. E. Meyerovich proposed that this analogy is richer and predicted that other phenomena observed in the dynamics of spin-polarized gases, including the Castaing instability, ought to be observable in trapped ultracold atomic systems [13]. J. N. Fuchs *et al.* [18] studied the presence of the Castaing instability quantitatively considering system parameters similar to

the experiment described in [6]. Based on these theoretical studies we designed an experiment to investigate the Castaing instability in a trapped two-component ^{87}Rb gas experimentally.

2.2.1 Quantum Boltzmann transport equation

Spin dynamics in spin-polarized systems are described using a quantum Boltzmann transport equation [8, 9, 10, 11]. As the trapped atomic cloud in our experiment is highly elongated along one axis (z) and the radial trap frequency is high compared to other relevant experimental time scales, we average the sample over the radial dimensions of the sample and treat the dynamics as being one-dimensional (1D).

The one-dimensional time evolution of the phase-space spin distribution function $\vec{\sigma}(p, z, t)$ is described by the quantum Boltzmann transport equation

$$\frac{\partial \vec{\sigma}}{\partial t} + \frac{p}{m} \frac{\partial \vec{\sigma}}{\partial z} - \frac{\partial U_{\text{ext}}}{\partial z} \frac{\partial \vec{\sigma}}{\partial p} - \vec{\Omega} \times \vec{\sigma} = \left. \frac{\partial \vec{\sigma}}{\partial t} \right|_{1D}, \quad (2.6)$$

where the first three terms represent the total time derivative of $\vec{\sigma}(p, z, t)$, U_{ext} is the external magnetic trapping potential, and p and z are momentum and position, respectively [9]. The collisional damping term on the right-hand side is proportional to the scattering probability, which is quadratic in scattering length. $\vec{\Omega} \times \vec{\sigma}$ is the spin rotation term, where $\vec{\Omega}$ is the coupling field that contains the spin interaction term

$$\vec{\Omega} = \frac{1}{\hbar} \left(U_{\text{diff}} \hat{W} + g \vec{S} \right). \quad (2.7)$$

U_{diff} is the differential potential between the spin states and $g = 4\pi\hbar^2 a_{ij}/m$ for an atom with mass m and scattering length a_{ij} , which is the s-wave scattering length between atoms in states $|i\rangle$ and $|j\rangle$ ($i, j = 1, 2$). For ^{87}Rb the scattering lengths are approximately equal. $\vec{S}(z, t)$ is the spatial distribution of the total spin

$$\vec{S}(z, t) = \frac{1}{2\pi\hbar} \int dp \vec{\sigma}(p, z, t), \quad (2.8)$$

which is the experimentally measurable quantity. It is clear that due to the spin interaction term in Eq. 2.6 the spin dynamics are nonlinear in these systems.

2.2.2 Collective behavior in atomic collisions

The spin rotation term in the transport equation (Eq. 2.6) is due to a quantum mechanical effect occurring during collisions between indistinguishable particles. This rotation is due to the exchange symmetry in collisions between indistinguishable particles in a quantum gas with different spin orientation. While this effects would work for a Fermi gas as well, we study a Bose gas in our experiments (see Chapter 3). The symmetrization of the scattered wave function between forward and backward scattering results in the rotation of the spin of each interacting particle around the combined total spin [7]. Figure 2.3 shows (a) the forward and (b) the backward scattering events in a collision between two indistinguishable particles, which leads to the rotation of the spins as demonstrated in Fig. 2.4. This rotation is referred to as the identical spin rotation effect (ISRE) in [7]. The ISRE for a spin- $\frac{1}{2}$ system can be considered as a rotation of the spin around an effective magnetic field.

Theoretical studies used the ISRE to explain the spin-state segregation in the JILA experiment [6], describing it as an initial onset of a spin wave oscillation [8, 9, 10, 11]. The situation in that experiment is such that a coherent superposition of the two spin states, corresponding to a uniform transverse pseudo-spin profile in the Bloch representation, is prepared by applying a $\pi/2$ pulse to the system initialized in state $|1\rangle$. Because of the inhomogeneity in the trapping differential potential the transverse spin precession rate depends on the position of the atoms in the trap. As a result an inhomogeneity in the transverse spin profile is created across the sample (Fig. 2.5). The atoms are moving in the trap, and due to the inhomogeneity in the transverse spin profile they enter regions with a different transverse spin orientation compared to their transverse spin, leading to the ISRE in the collisions between these atoms. Since the net spin is in the transverse plane, the ISRE rotates the spin of particles out of the transverse plane generating longitudinal spin components. These spin components have opposite signs for atoms with opposing velocities [8], leading to the subsequent separation of the two internal states. It should be noted that this separation is not a spatial separation of atoms in fixed internal states.

2.2.3 Spin waves and the Castaing instability

Quantitative studies for spin polarized helium systems in the hydrodynamic regime using the spin transport equation (Leggett equation) [13] demonstrate that in a system with a homogeneous longitudinal spin distribution, S_{\parallel}^0 , a smoothly varying transverse inhomogeneity $\delta\vec{S}_{\perp}$ leads to the gener-

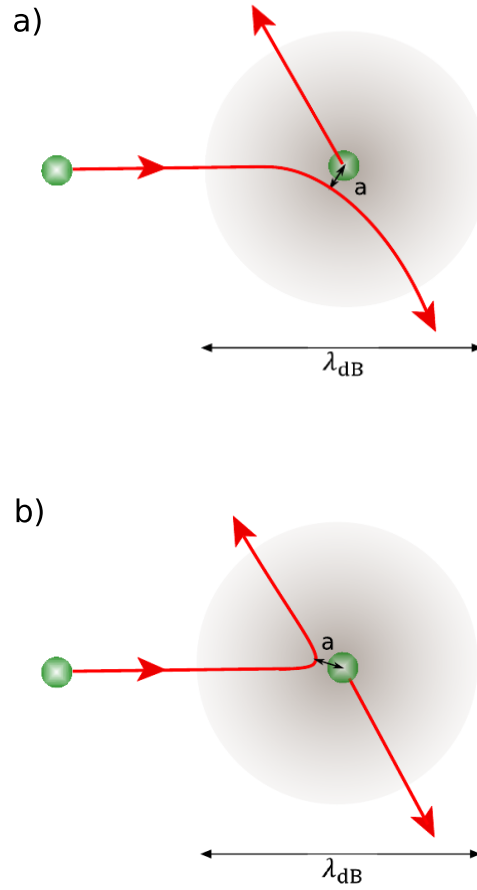


Figure 2.3: Schematic depiction of two identical atoms colliding with each other. As the thermal de Broglie wavelength (λ_{dB}) is larger than the scattering length (a), the two scattering events, (a) forward and (b) backward scattered events are indistinguishable.

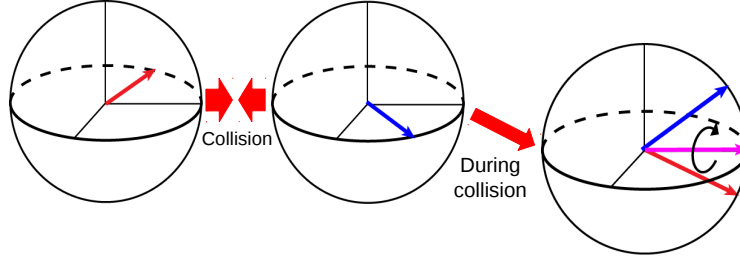


Figure 2.4: Schematic illustration of the spin rotation in a collision between two indistinguishable particles, using the Bloch sphere representation. The two Bloch spheres on the left represent two particles with slightly different transverse spin colliding with each other. As a result of the ISRE, the spin of each particle rotates around the total spin during the collision, which is conserved.

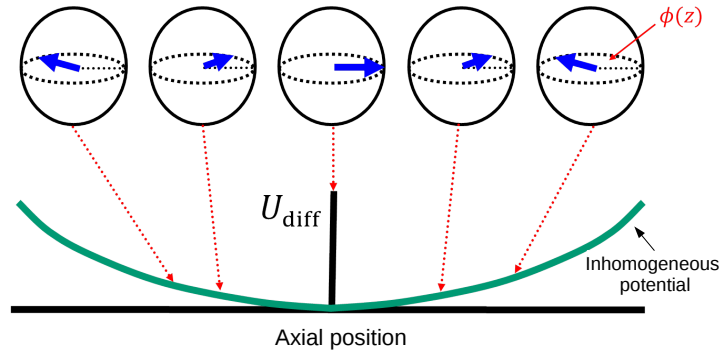


Figure 2.5: The inhomogeneous differential potential U_{diff} in the trap leads to spatially dependent precession rates for the transverse spin. The atoms in different positions in the trap are represented as Bloch spheres with spatially dependent transverse spin phase ϕ . As a result of the varying transverse spin precession rate, an inhomogeneity is created in the transverse spin profile.

ation of spin waves. In reference [13] an initial spin profile given as

$$\vec{S} = S_{\parallel}^0 \hat{W} + \delta \vec{S}_{\perp} e^{i(kz - \omega t)}, \quad (2.9)$$

in which the transverse perturbation is considered as a plane wave with wave vector k , is substituted in the transport equation. Assuming that the sample has a uniform density distribution (which is a good assumption for spin polarized He samples) and short range interactions leads to the following spectrum for spin waves

$$\omega = \frac{Dk^2}{1 + \mu^2 S_{\parallel}^0{}^2} (i - \mu S_{\parallel}^0), \quad (2.10)$$

where $D = k_B T \tau / m$ is the spin diffusion coefficient (T is the temperature and τ is the diffusive spin relaxation time), and $\mu = 2gn(0)\tau/\hbar$ is the spin rotation parameter for an atomic cloud with the peak density $n(0)$. μ is the parameter that characterizes the ISRE strength.

B. Castaing in his studies of spin-polarized ^3He gas in [19] showed that a small transverse inhomogeneity ($\delta \vec{S}_{\perp}$) added to a purely longitudinal spin distribution with a nonequilibrium longitudinal gradient ($\nabla S_{\parallel} \neq 0$), as shown in Fig. 2.6, results in an instability in the transverse spin component due to an additional term in the imaginary part of the dispersion relation, which now becomes

$$\text{Im}(\omega) = \frac{D}{1 + \mu^2 S_{\parallel}^0{}^2} \left(k^2 - 2\mu \vec{k} \cdot \vec{\nabla} S_{\parallel}^0 \frac{\mu^2 S_{\parallel}^0{}^2}{1 + \mu^2 S_{\parallel}^0{}^2} \right). \quad (2.11)$$

In Eq. 2.11, for wave vectors satisfying

$$k^2 < 2\mu \vec{k} \cdot \vec{\nabla} S_{\parallel}^0 \frac{\mu^2 S_{\parallel}^0{}^2}{1 + \mu^2 S_{\parallel}^0{}^2}, \quad (2.12)$$

the imaginary part of the dispersion relation has a negative sign, resulting in an instability in the transverse spin channel manifested as a rise in the magnitude of the initial transverse perturbation. This instability is called the Castaing instability after his work.

It should be noted that trapped atomic samples are different from spin polarized He systems, mainly due to the presence of a trapping potential and nonuniform density distribution, and the aforementioned analytical discussion does not exactly match trapped atomic systems. However, numerical studies of the quantum Boltzmann transport equation, Eq. 2.6, carried out by J. N. Fuchs

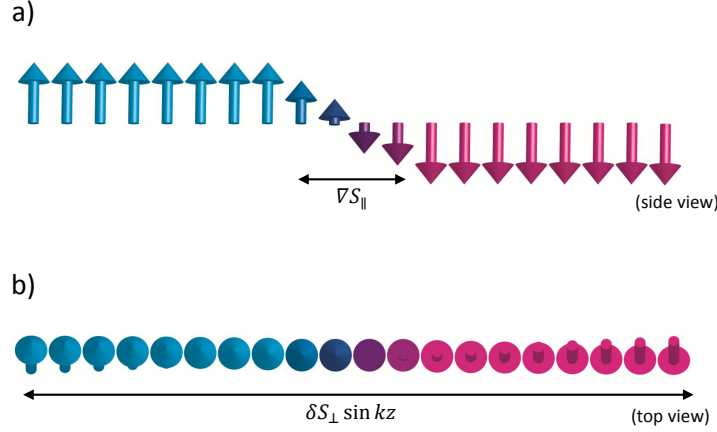


Figure 2.6: Schematic illustration of a longitudinal spin profile containing a gradient. (a) Side view showing the longitudinal spin gradient ∇S_{\parallel} in the middle. (b) Top view showing the small transverse perturbation $\delta S_{\perp} \sin kz$.

et al. [18], using experimental parameters of trapped atomic gases, such as density, scattering length, spin rotation strength, etc., showed that the instability can develop in such systems.

The spin-state segregation observed in [6] did not involve the Castaing instability since there was a large transverse spin component present after initializing the system, as a result of the first $\pi/2$ pulse applied. However, if there is a sufficient nonuniformity in the initial transverse spin profile, an instability in the longitudinal spin component can also occur, which results in a faster component separation compared to [6]. We examined this condition experimentally by imprinting a sharp spin gradient in the transverse spin profile.

According to discussions in [13], the Castaing instability in the longitudinal spin component can be described as the time reversal of the spin-state segregation in [6]. In that situation, the initial nonuniform transverse spin profile leads to the separation of the two components, but in the Castaing phenomenon, transverse spin is created as a result of the instability during the component mixing.

In a trapped atomic system the wave vectors k are bounded by the presence of the trap. That is, the size of the system (L) constrains the allowed wave vectors, imposing $k > \pi/L$. For a fully polarized system, the homogeneous region away from any gradient has $S_{\parallel}^0 = \pm 1$. The spin rotation parameter in our system is $\mu \sim 6$ (for $T = 600$ nK and $a = 5.18 \times 10^{-9}$ m). Starting from

Eq. 2.11, considering that $(\mu S_{\parallel}^0)^2 \gg 1$ and the dynamics are one dimensional, sets the criterion for the observability of the Castaing instability as

$$2\mu \nabla S_{\parallel}^0 > \frac{\pi}{L}. \quad (2.13)$$

We are capable of creating longitudinal spin gradients with a length scale of $l_{\nabla S_{\parallel}} \simeq 1.1 w_z$ (see Section 4.2.2), where w_z is the Gaussian half-width of the trapped atomic cloud in the axial dimension (*i.e.* $L = 2w_z$). It is clear that these parameters, *i.e.* $\nabla S_{\parallel} = \frac{1}{l_{\nabla S_{\parallel}}}$ and $\mu \sim 6$, are consistent with the instability criterion (Eq. 2.13); therefore it is conceivable to observe the Castaing instability in the spin configuration we prepare. The results of the Castaing instability experiment in both transverse and longitudinal spin channels are presented in Chapter 5.

Chapter 3

Experimental design

This chapter gives an overview of the experimental setup used in this research. We are working with a Bose-Einstein condensation apparatus, but for these experiments we studied nondegenerate samples rather than condensates. For the experiments presented in this thesis we work with samples of a quantum gas, trapped ultracold ^{87}Rb atoms (a composite boson) at a temperature of 600 nK ($T = 1.1 T_c$).

Different systems are used to create Bose-Einstein condensates of different atomic species using various sorts of trapping and cooling techniques. Our apparatus is designed based on the work of H. J. Lewandowski *et al.* [20], which was an attempt to create a simplified BEC machine designed to "*consistently produce a stable condensate even when it is not well optimized*", as they claimed. I will start by giving an overview of our BEC system and then proceed with describing different parts in more detail.

For creating a BEC we first trap and cool ^{87}Rb atoms in a magneto-optical trap (MOT), and then transfer them to an ultra-high vacuum (UHV) science cell, where the atoms are confined in the harmonic potential of an Ioffe-Pritchard magnetic trap. In the science cell, evaporative cooling cools the atoms into quantum degeneracy. The condensate is finally imaged using a shadow imaging technique. These images are used to extract the atomic cloud properties such as spatial distribution, number and temperature.

This procedure requires using lasers of different frequencies. We need two lasers to trap the atoms in the MOT (cooling laser and repumper laser), and then we image the condensate with another one (probe laser). We use three different external cavity diode lasers (ECDLs) for these tasks.

3.1 Magneto-optical trap (MOT)

A combination of laser cooling and inhomogeneous magnetic fields can be used to trap neutral atoms [14]. The idea of laser cooling is to use a laser beam tuned below an atomic resonance transition. During the process of absorption and reemission of a photon from this off-resonant beam, atoms experience a momentum kick. The atoms moving towards the beam see the laser frequency closer to the transition resonance due to the Doppler shift, which leads to a higher scattering rate. Since the photon reemission is isotropic, the whole process will lead to slowing down the atoms that are moving towards the laser beam, as they scatter photons at a higher rate.

By means of laser cooling, atoms can be cooled and confined in three dimensions in an optical molasses (OM) setup by shining six laser beams that are counter-propagating to each other, with each pair along one of the spatial dimensions. An OM setup is not a trap for neutral atoms since there is no restoring force for the atoms displaced from the center [14]. Position-dependent forces can be added using inhomogeneous magnetic fields. A magnetic field shifts the atomic energy levels due to the Zeeman effect. These energy shifts depend on the Zeeman sublevel labeled by m_f (m_f is the magnetic quantum number), and conservation of angular momentum makes the photon absorption polarization dependent.

In a MOT, a pair of electromagnetic coils in an anti-Helmholtz configuration produces a quadrupole magnetic field. This magnetic field creates a linear potential that is zero in the center of the trap, as shown in Fig. 3.1. By shining two counter-propagating laser beams with opposite circular polarization the atoms are pushed towards the center of the trap, where the magnetic field is zero. Using six counter propagating beams instead of two, this trapping scheme can be expanded to three dimensions (Fig. 3.2).

MOTs are very robust traps with easy operation, which can be used to produce atomic samples with μK temperatures. Commercially available diode lasers have appropriate frequencies for trapping most Alkali atoms, including Rb.

The number of trapped atoms in a MOT is limited by reabsorption of spontaneously emitted photons. Due to this process the density in a MOT is limited to $\sim 10^{11} \text{ cm}^{-3}$. We trap 3×10^9 atoms in our MOT at a temperature of $T = 300 \mu\text{K}$.

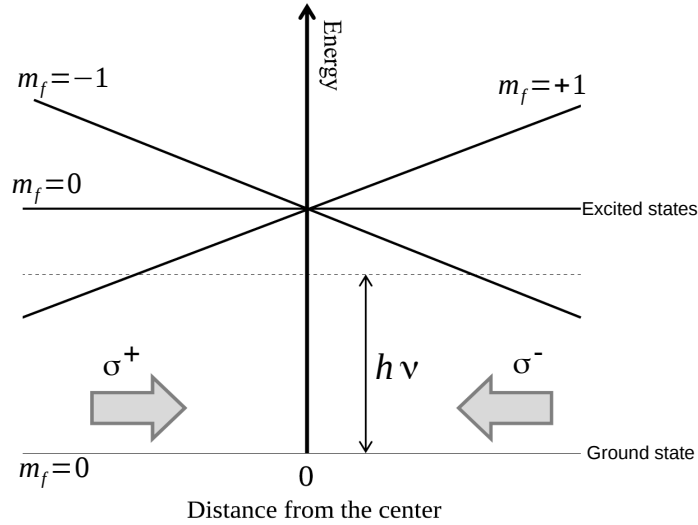


Figure 3.1: Trapping process in a 1D MOT. The atomic excited state is Zeeman-shifted in the magnetic field. The dashed line indicated on the diagram represents the energy of the incoming photon ($h\nu$) detuned from ground-to-excited state transition. On the right side, the incident laser frequency is closer to the transition from the ground state to the $m_f = -1$ excited state, as the $m_f = -1$ state is shifted down due to the Zeeman shift. Therefore the transition with $\Delta m = -1$ is closer to be resonant with the illuminating laser and the atoms on that side scatter σ^- photons at a higher rate than the σ^+ photons. Choosing the right polarization of the incident beams leads to driving the atoms towards the center of the trap.

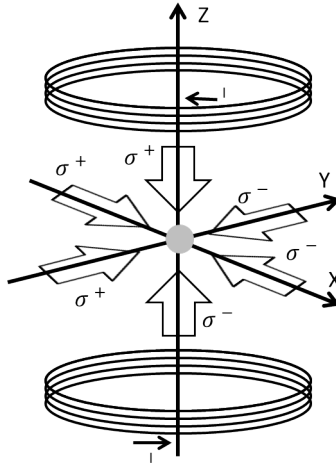


Figure 3.2: MOT setup. A pair of electromagnetic coils in anti-Helmholtz configuration produces a quadrupole magnetic field. Counter-propagating laser beams with opposite polarization are used to confine the atoms in three dimensions.

3.2 Lasers and locks

Figure 3.3 shows the hyperfine structure of the D_2 transition ($5^2S_{1/2} \rightarrow 5^2P_{3/2}$) of ^{87}Rb in zero magnetic field [21]. We use different transitions to achieve different goals. We tune our cooling laser in the MOT to the $F = 2 \rightarrow F' = 3$ transition, where the prime notation refers to an excited state and F denotes the total angular momentum of a hyperfine level. Due to off-resonant transitions some atoms can be excited to the $F' = 2$ state and decay back to the $F = 1$ hyperfine level, which is not in the trapping cycle. A different laser (repumper laser) tuned to the $F = 1 \rightarrow F' = 2$ transition is used to force the atoms back into the cooling cycle.

In our experimental setup, two different methods are used to lock lasers to the desired transitions. We use the saturated absorption spectroscopy (SAS) method to lock the MOT beams. A phase-locked loop (PLL) setup is used to lock our probe laser for imaging atoms as well as the phase imprinting laser for driving spin dynamics. I will briefly explain the principles of these locking techniques in the following sections.

3.2.1 Saturated absorption spectroscopy

Saturated absorption spectroscopy is a technique used to remove Doppler line-broadening effects on an atomic transition by velocity-selective absorption. The sub-Doppler spectral lines generated using this technique can be applied in stabilizing the laser frequency [22].

In this technique, two almost counter-propagating beams from the same laser, a weak probe beam and a strong pump beam, pass through a vapor cell as indicated in Fig. 3.4. The probe beam's spectrum has a Doppler-broadened absorption profile. Far from a resonance, the absorption of the pump beam does not affect the probe absorption, as they address different velocity groups of atoms due to the Doppler effect. But at resonance the strong pump beam excites many atoms into the upper atomic level, decreasing the absorption of the probe beam (hole burning). Using this procedure we can locate the resonant frequency by looking for the intensity variations of the probe beam on a photodiode.

Figure 3.4 shows the schematic of our saturated absorption spectroscopy setup. Spectral lines can be viewed by scanning the laser frequency across the atomic transitions. In a SAS spectrum for multi-level atoms, some extra peaks occur at frequencies halfway between two transitions (cross-over resonances). These peaks are usually better signals to lock to, as they are stronger. We lock the MOT's cooling laser to the $3' - 2'$ cross-over resonance halfway between the $F = 2 \rightarrow F' = 2'$ and

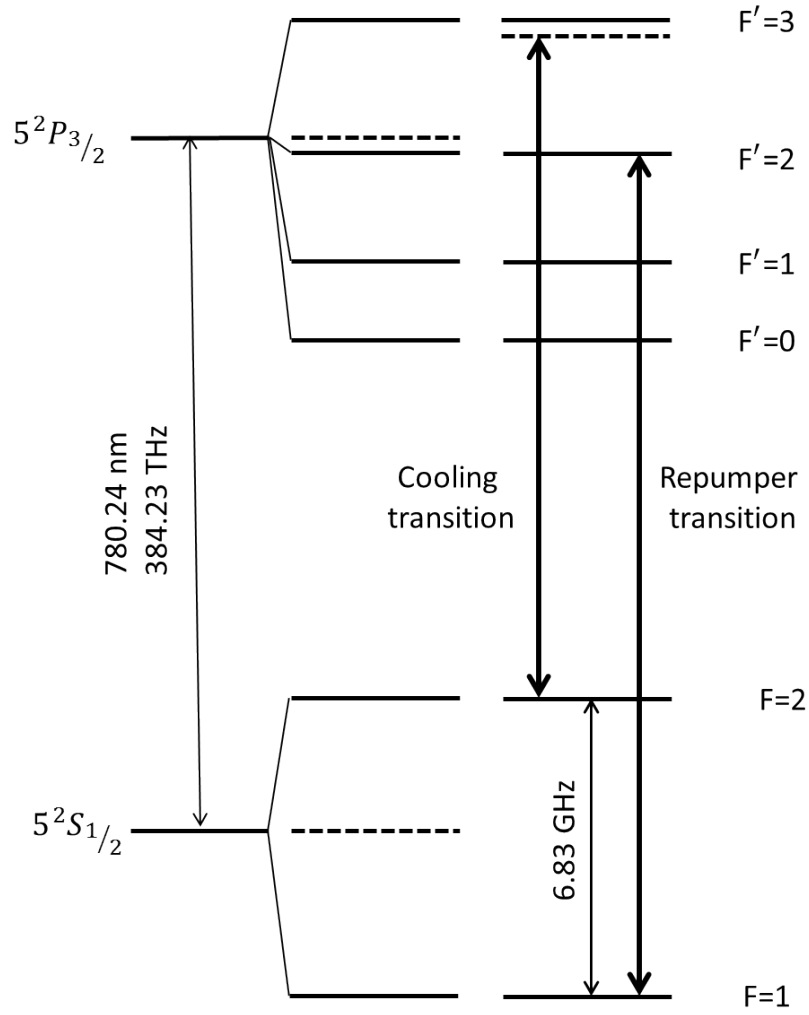


Figure 3.3: Schematic representation of the hyperfine structure of the D_2 transition ($5^2S_{1/2} \rightarrow 5^2P_{3/2}$) of ^{87}Rb in zero magnetic field. The cooling transition ($F = 2 \rightarrow F' = 3$) and repumper transition ($F = 1 \rightarrow F' = 2$) are indicated on the diagram.

$3'$ transitions. Figure 3.5a [23] shows absorption spectral lines for ^{87}Rb . Modulating the frequency of the pump beam with an acousto-optical modulator (AOM) allows us to produce an error signal (Fig. 3.5b), which can then be used in stabilizing the laser frequency.

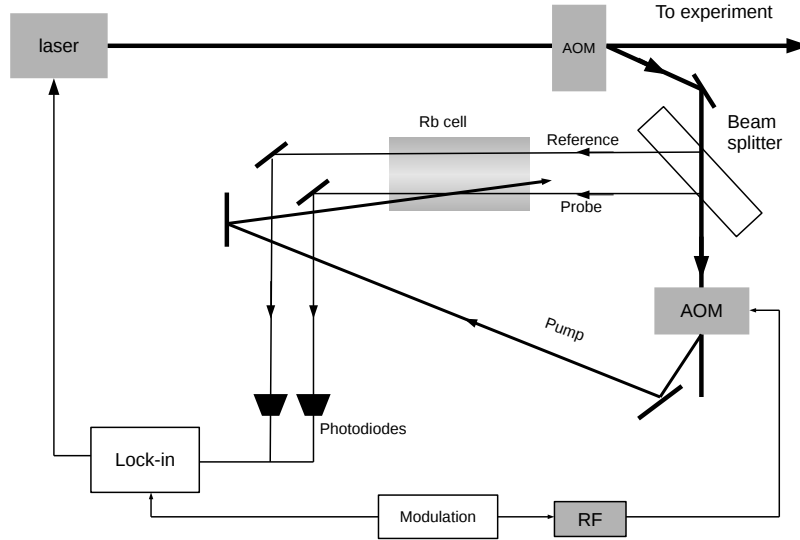


Figure 3.4: Schematic of our SAS setup. Counter-propagating pump and probe beams from the same laser separated by a beam splitter pass through a Rb vapor cell. The absorption profile of the probe beam is compared to a reference beam. An error signal is sent back to the laser controller. Arrows show the beam directions.

3.2.2 Phase-locked loop

In this locking technique a laser is stabilized by comparing its frequency to a fixed reference frequency using a phase-frequency detector. Electronic devices cannot process optical frequencies; therefore to apply this technique for stabilizing a laser we mix our laser beam with another beam with a fixed frequency. Mixing the two laser beams results in beatnotes at frequencies of the sum and difference of the two mixed beams. This stage of the locking procedure allows us to stabilize the laser frequency to another optical frequency with a desired detuning.

Figure 3.6 shows the PLL setup schematically. The beatnote signal is mixed with an rf signal from a local oscillator (LO), and the high frequency component of the mixed signal is removed using a low-pass filter. A phase-frequency detector compares this signal to a fixed reference frequency

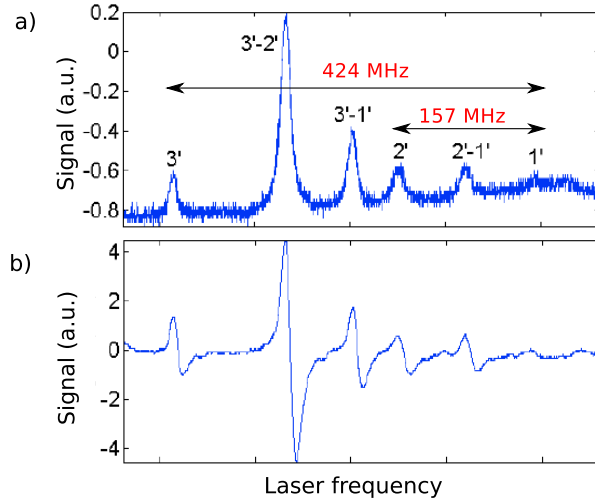


Figure 3.5: (a) Absorption spectral lines of ^{87}Rb for the $F = 2 \rightarrow F' = 1', 2'$ and $3'$ and cross-over transitions. (b) Error signal for the $F = 2 \rightarrow F' = 1', 2'$ and $3'$ and cross-over transitions. Image courtesy of R. Thomas.

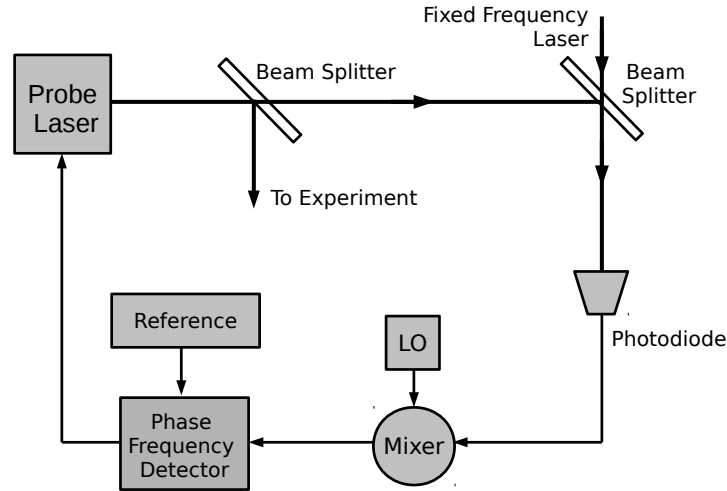


Figure 3.6: Schematic of our PLL setup. The laser beam is mixed with another laser beam with a known fixed frequency. Some arrows indicate beam direction. The resulting beatnote is collected on a photodiode and mixed with a local oscillator (LO) signal. The phase-frequency detector compares this signal to a reference, and the error signal is sent back to the laser controller to modify the laser frequency. The locked laser's linewidth is well below the transition linewidth of 6 MHz.

and generates an error signal that is sent back to the laser controller. This technique gives us the flexibility to select the laser frequency simply by adjusting the frequency of the local oscillator.

3.3 Magnetic trap

After being cooled in the MOT, the atomic sample is transferred to a purely magnetic trap for further cooling via radio frequency (rf) induced evaporative cooling. Magnetic trapping of neutral atoms requires an interaction between the atomic magnetic moment and inhomogeneous magnetic fields. In an inhomogeneous magnetic field \vec{B} , an atom with dipole moment $\vec{\mu}$ experiences a force equal to

$$\vec{F} = \vec{\nabla} \left(\vec{\mu} \cdot \vec{B} \right). \quad (3.1)$$

Appropriate magnetic field configurations can be used to create a minimum in the magnetic potential in order to trap neutral atoms. Various magnetic trap configurations for neutral atoms have been studied, some of which are discussed in [24].

3.3.1 Ioffe-Pritchard trap

The magnetic trap in our experiment is slightly different than a standard Ioffe-Pritchard trap [25]. Our trap consists of a pair of permanent magnets and four electromagnetic coils. This trap is referred to as a hybrid Ioffe-Pritchard (HIP) trap (Fig. 3.7). In this configuration instead of Ioffe bars the permanent magnets provide radial confinement without any power consumption. They produce a radial quadrupole field in the center of the trap (Fig. 3.8). Axial confinement is then produced by two pairs of electromagnetic coils. There are two pinch coils (outer pair) that produce axial curvature in magnetic field. Two bias coils (inner pair) in a Helmholtz configuration produce a uniform magnetic field B_0 in the center. The magnitude of the resulting magnetic field $|\vec{B}|$ is

$$|\vec{B}| \approx \sqrt{(\eta\rho)^2 + \left(B_0 + \frac{\beta}{2}z^2 \right)^2}, \quad (3.2)$$

where η is the radial field gradient produced by the permanent magnets (ρ is the radial position) and β is the axial curvature produced by the pinch coils (z is the axial position). At low magnetic fields the magnetic trapping potential near the center of the trap can be approximated as a cylindrically

symmetric anisotropic harmonic potential [25]

$$U \approx \frac{m}{2} (\omega_r^2 \rho^2 + \omega_z^2 z^2). \quad (3.3)$$

The radial frequency ω_r and the axial frequency ω_z are

$$\omega_r = \sqrt{\frac{m_f g_f \mu_B}{m B_0}} \eta \quad (3.4)$$

and

$$\omega_z = \sqrt{\frac{m_f g_f \mu_B \beta}{m}}, \quad (3.5)$$

where g_f is the Landé g -factor, μ_B is the Bohr magneton and m is the mass of Rb atoms. In our experiment the trap frequencies are $\omega_z = 6.7$ Hz and $\omega_r = 247$ Hz (Fig 3.9). The trapped atomic cloud has an ellipsoidal geometry that is highly elongated along the axial direction with typical gaussian widths of $10 \times 10 \times 380$ μm ; therefore this atomic sample can be treated as a one-dimensional system.

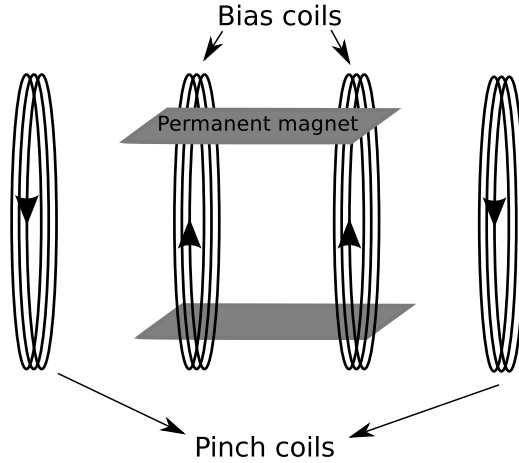


Figure 3.7: Hybrid Ioffe-Pritchard trap. Opposite currents pass through the pinch and bias coils. The bias coils are in a Helmholtz configuration, producing a uniform magnetic field in the center of the trap.

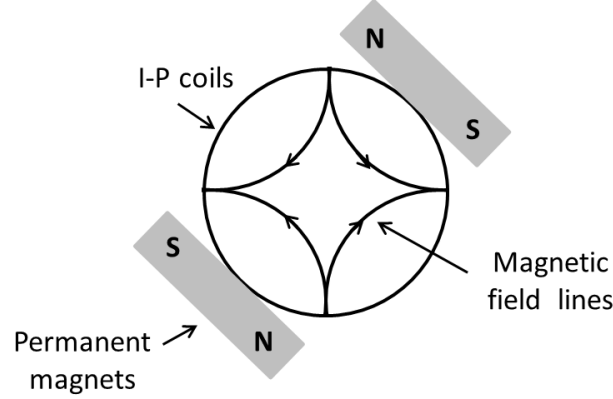


Figure 3.8: HIP trap end-on view. This configuration of permanent magnets produces a radial quadrupole field and no field along the axial direction.

3.3.2 From the MOT to the HIP trap

Using a moving magnetic trap we transfer the atoms collected in the MOT to the UHV science cell, where they are trapped in the HIP trap. In order to accomplish this task we first load the atoms into a "tight" quadrupole trap, which holds the trapped atoms during the mechanical transfer between the MOT cell and the science cell. This tight confinement is attained by increasing the magnetic field gradient relative to its value in the MOT, which in turn increases the Zeeman shift of the atomic energy sublevels as one moves away from the trap center. In other words, the quadrupole magnetic field energy increases linearly with radial position, and so atoms near the edge of the atomic cloud have the largest Zeeman shifts. Most of the resultant energy for the trapped atoms in a magnetic trap comes from the potential energy due to this Zeeman shift [20]. This effect would add less energy to the system for a smaller cloud; therefore it is desirable to reduce the size of the trapped atomic cloud prior to loading the atoms into the quadrupole trap. This task is accomplished in a stage referred to as compressed MOT (CMOT) subsequent to trapping in the MOT.

During the CMOT stage the atomic cloud is made smaller by detuning the cooling and the repumper light [26]. The time that atoms spend in the upper hyperfine ground state ($F = 2$, resonant with the cooling light) is reduced by detuning the repumper frequency. Furthermore, increasing the

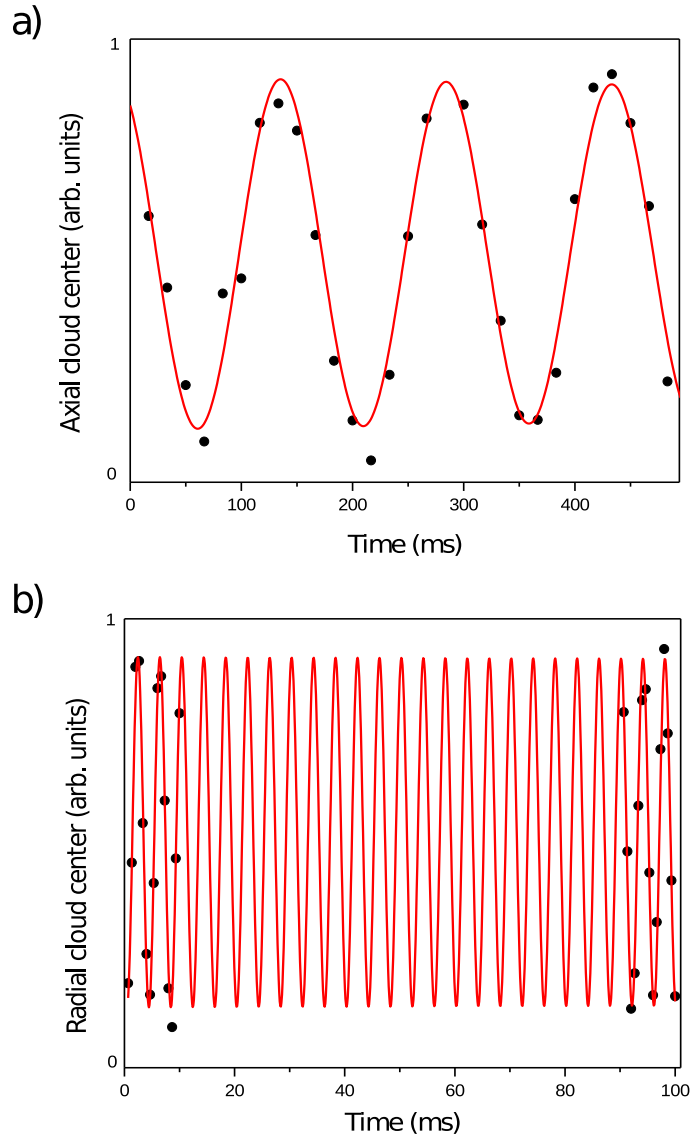


Figure 3.9: (a) Axial and (b) radial trap frequency measurement data. Using an extra electromagnetic coil placed near the trap, axial or radial oscillations are induced in the trap. The position of the center of the trapped atomic cloud is measured as a function of time to extract the trap frequencies.

detuning of the cooling laser decreases the absorption and reemission of light, leading to a reduction of the radiation pressure and a smaller cloud size.

We also need to optically pump the atoms into a magnetically trappable hyperfine state. These are the states whose energy increases as the magnetic field is increased. The magnetically trappable hyperfine sublevels for the ground state of ^{87}Rb in low magnetic fields ($B \leq 1000$ G) are $|1, -1\rangle$, $|2, 1\rangle$ and $|2, 2\rangle$ (Fig 3.10 [21]). $|F, m_f\rangle$ denotes a hyperfine quantum state with total angular momentum F and magnetic quantum number m_f . All the atoms will be pumped into the $F = 2$ state if the cooling light is turned off. However, in the $F = 2$ hyperfine state the population of the atoms would be divided between the five Zeeman-shifted m_f sublevels. The atoms will be pumped into the $F = 1$ hyperfine state if the repumper light is turned off and the cooling light is left on. To obtain higher population in each state we turn off the repumper light to pump the atoms into the $F = 1$ hyperfine state. The atoms in the $|1, -1\rangle$ sublevel will be trapped in the HIP trap after being transferred to the science cell.

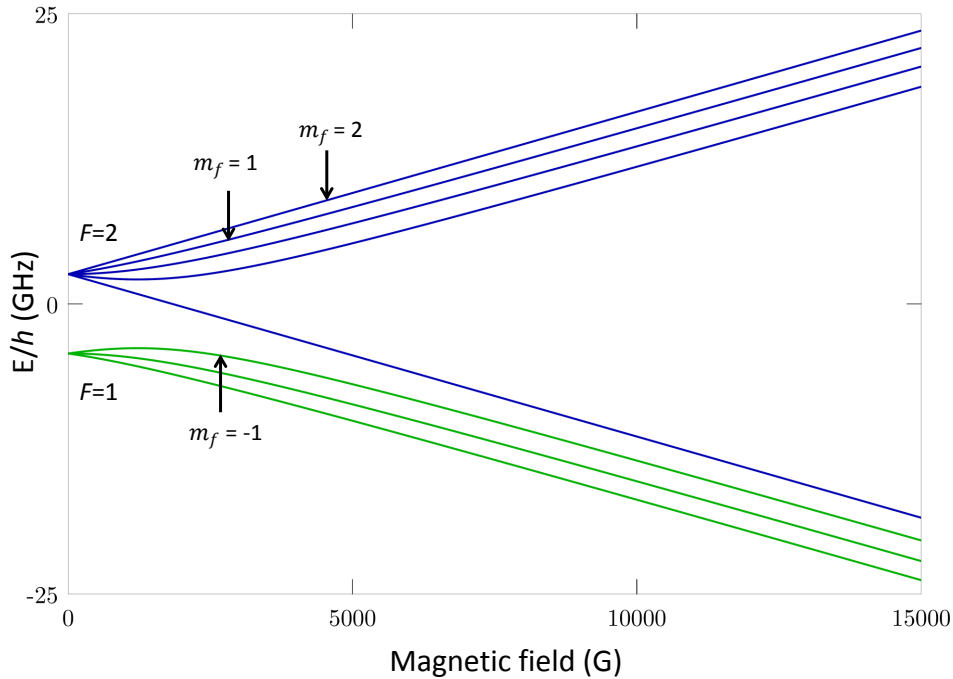


Figure 3.10: Zeeman-shifted ^{87}Rb hyperfine splitting in a magnetic field. It is evident that in low magnetic fields, the energy of the $|1, -1\rangle$ state increases with magnetic field.

3.4 Evaporative cooling

We use rf-induced evaporative cooling to cool the atoms confined in the HIP trap near or into quantum degeneracy. The principle of evaporative cooling is to remove atoms with higher energies than the average energy of the atomic sample and allow the sample to rethermalize through elastic collisions to a lower temperature [14].

In our experiment we use transitions to untrapped Zeeman levels to remove atoms from the trap in order to evaporatively cool the sample. Atoms with lower energies are on average closer to the center of the trap and have smaller Zeeman shifts. The high energy atoms can reside in regions with higher magnetic fields, farther from the center of the trap where the Zeeman shift is larger. By applying rf radiation tuned to transitions from the $|1, -1\rangle$ state to the untrapped $|1, 0\rangle$ state, atoms are ejected from the trap carrying away energy. Thus, by sweeping the rf frequency from high to low we can target atoms selectively from high to low energies and cool the atomic cloud. As long as the atom-loss rate is not too fast, this process will lead to an increase in the phase-space density since the atoms with lower energies occupy the space closer to the center of the trap.

We use a single-loop rf coil placed below the science cell to deliver rf radiation to the trapped atoms, and sweep the rf frequency from 60 MHz to around 3 MHz. We use an exponentially decreasing frequency ramp with the functional form [20]

$$\nu(t) = (\nu_{\text{start}} - \nu_0) e^{-t/\tau} + \nu_0, \quad (3.6)$$

where ν_{start} is the initial rf frequency at the start of the evaporation, ν_0 is the trap bottom frequency and τ is the time constant of the exponential ramp.

As the elastic collision rate varies during evaporation because of changes in density and temperature of the atomic cloud, the evaporation process needs to be carried out in several stages with an accordingly modified time constant for each stage. The total time of all ramps is 1 minute. To optimize the evaporation process, we modify the rf power and the time constant of the exponential ramp for each stage of the evaporation. The time constant needs to be longer than the elastic collision time in order for the sample to remain in thermal equilibrium. A higher rf power level increases the probability of a transition, yet it causes power broadening, which decreases the energy selectivity of the process. Thus we start with higher powers and decrease the power by 20 dB for the last steps of the evaporation.

3.5 Imaging

We measure the population of the atoms trapped in the $|1, -1\rangle$ state using an absorption imaging technique. In this procedure the atomic cloud is illuminated by a resonant probe beam tuned to an atomic transition. The atoms absorb the probe's light, producing a shadow of the atomic cloud, which is focused on a CCD camera. The optical density (OD) of the atoms can then be calculated using Beer's law

$$\text{OD} = \ln(I_0/I), \quad (3.7)$$

where I_0 is the probe beam intensity and I is the measured intensity when atoms are present. The number and temperature of the atoms are calculated using the spatial profile obtained from measured OD.

The atoms are trapped in the $|1, -1\rangle$ state in the HIP trap, but there is no cycling transition to the excited state for this state. It is preferable to use a cycling transition for imaging, as it increases the signal-to-noise ratio. Therefore, first we coherently transfer the atoms from $|1, -1\rangle \rightarrow |2, -2\rangle$ using an adiabatic rapid passage (ARP) technique [14], and then the $|2, -2\rangle \rightarrow |3, -3\rangle$ cycling transition is used for imaging.

Several systematic effects are important to consider during the imaging process. The atomic energy splitting changes across the atomic cloud due to the inhomogeneity in the trapping magnetic field. Thus the probe light cannot be resonant with the entire cloud. Imaging the atoms in a more uniform magnetic field minimizes this effect. To image the atoms we also need to expand the atomic cloud beyond the resolution limit of our CCD camera. Expanding the atomic cloud is also important to avoid high absorption [26]. We expand the atomic cloud in the anti-trapped $|2, -2\rangle$ state after being transferred from the $|1, -1\rangle$ state.

Figure 3.11 shows the Zeeman-shifted ground and excited states in ^{87}Rb in low magnetic fields and the imaging transitions. We start with the atoms in the $|1, -1\rangle$ state. The atoms are then transferred to the $|2, -2\rangle$ state in $t_{\text{ARP}} = 0.65$ ms. In the $|2, -2\rangle$ state, the cloud is expanded in an intermediate 50 G magnetic field. We do not perform the expansion in the initial 3 G field because the atoms will expand too quickly into inhomogeneous regions of the trap. We do not perform the expansion in the 100 G imaging field because the atoms will expand too slowly. The intermediate 50 G bias field is chosen because it allows us to keep the atomic cloud within the homogeneous region of the potential during the expansion. After proper expansion the bias field value is increased to 100 G and imaging pulses are applied.

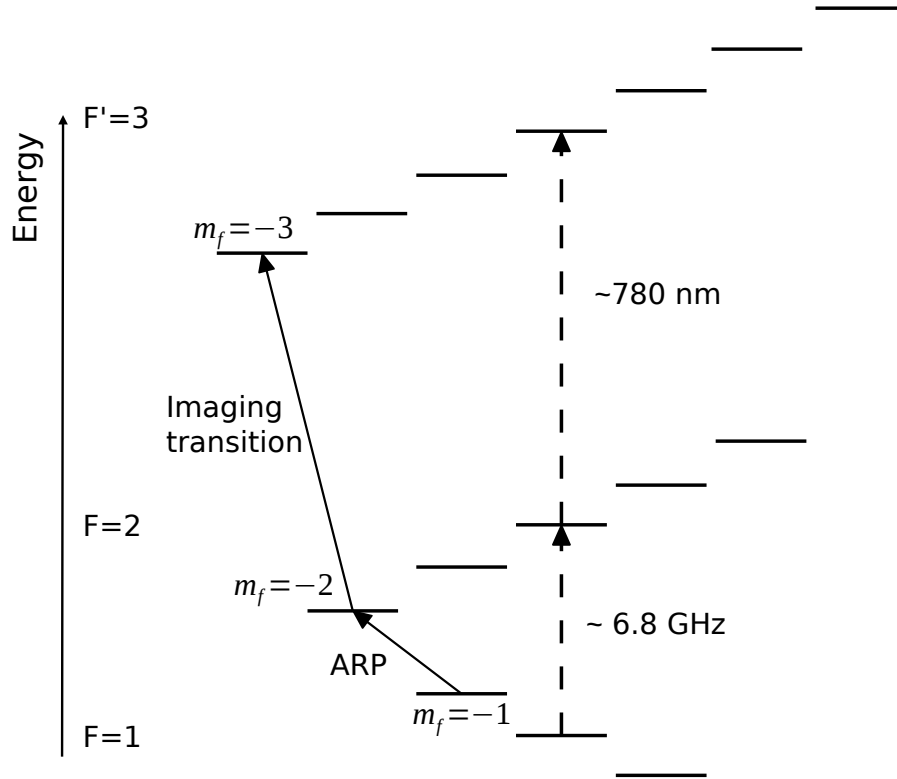


Figure 3.11: Schematic representation of the Zeeman-shifted ground ($5S_{1/2}$) and excited ($5P_{3/2}$) states of ^{87}Rb in low magnetic fields. The ARP ($|1, -1\rangle \rightarrow |2, -2\rangle$) and imaging ($|2, -2\rangle \rightarrow |3', -3\rangle$) transitions are shown on the diagram as solid arrows. The dashed arrows indicate the transitions for the $m_f = 0$ levels.

We take three images for normalization purposes. First, a shadow image is taken when the atoms are present (I_{shadow}). Second, while the probe light is on, a normalization image is taken without the atoms (I_{norm}). Finally a dark image (I_{dark}), which is subtracted from both the shadow and normalization images, is taken with no probe light present. The OD, which we denote OD_{meas} , is then calculated using

$$\text{OD}_{\text{meas}} = \ln \left(\frac{I_{\text{norm}} - I_{\text{dark}}}{I_{\text{shadow}} - I_{\text{dark}}} \right), \quad (3.8)$$

We also take into account the effects of systematic errors associated with absorption imaging. The first of these is that there is a maximum observable OD, which could be either due to scattered probe light that reaches the CCD camera but does not pass through the atomic cloud, or off-resonant probe light that passes through the atomic cloud but is not absorbed by the atoms. Using the PLL setup described in Section 3.2.2 to obtain a tight lock for the probe beam, we can decrease the amount of off-resonant light. To correct for any remaining effect we do the following. After measuring the maximum observable OD by imaging a very dense cloud expanded only for a short expansion time, we calculate a modified OD by

$$\text{OD}_{\text{mod}} = \ln \left(\frac{1 - e^{-\text{OD}_{\text{sat}}}}{e^{-\text{OD}_{\text{meas}}} - e^{-\text{OD}_{\text{sat}}}} \right). \quad (3.9)$$

There is a second saturation effect related to saturation of the imaging transition because of the probe beam intensity. To correct for this effect we use

$$\text{OD}_{\text{actual}} = \text{OD}_{\text{mod}} + (1 - e^{-\text{OD}_{\text{mod}}}) \frac{I}{I_{\text{sat}}}, \quad (3.10)$$

where I_{sat} is 1.67 mW/cm^2 . Even with the corrections it is desirable to work away from saturation limits; therefore we expand the atomic cloud to avoid observing a saturated OD and set the probe intensity to $I \sim \frac{1}{10} I_{\text{sat}}$.

We fit the image to three different functions depending on the degeneracy of the atoms in order to infer the atomic cloud properties. For normal clouds a 2-D Gaussian is fit to the image to extract the number, temperature and phase-space density using the fit parameters. We use the procedures described in [26]. More details on calculations of cloud parameters can be found in the aforementioned reference. Although we are capable of producing BECs with the described apparatus, for the experiments presented in this thesis we stop the evaporation above degeneracy. We use near degen-

erate atomic clouds with 7×10^6 atoms, peak density $n = 8.6 \times 10^{19} \text{ m}^{-3}$ and typical temperatures $T \simeq 600 \text{ nK}$ ($T \simeq 1.1 T_c$).

Chapter 4

Spin-state preparation

In the first part of this chapter I will first describe the experimental spin system. The experimental procedures used in preparing desirable spin profiles via the ac Stark effect will then be discussed. Finally the spin profile created in order to search for the Castaing instability will be presented and characterized at the end of this chapter.

4.1 The experimental pseudo-spin $\frac{1}{2}$ system

The Rabi two-level problem describes the behavior of a two-level system coupled via an oscillating electromagnetic field as previously discussed in Chapter 2. We consider two of the magnetically trapped hyperfine levels of the ground state ^{87}Rb atom, $|1, -1\rangle$ and $|2, 1\rangle$, as a two-level (pseudo-spin $\frac{1}{2}$) system ($|1\rangle \equiv |1, -1\rangle$ and $|2\rangle \equiv |2, 1\rangle$). A two-photon microwave transition (a 6.8 GHz microwave photon and a 3 MHz rf photon) couples the two states. The transition cannot be induced by a single photon, as the two states are different by two units of angular momentum. Both transitions are detuned from the $|2, 0\rangle$ state by 700 kHz to avoid transitions to the intermediate state. Figure 4.1 shows the Zeeman-shifted hyperfine structure of the ground state in ^{87}Rb in low magnetic fields, the sublevels taken as the pseudo-spin system and the related transitions.

The state of the system in an equal coherent superposition of the two spin states is given by

$$\psi = \frac{1}{\sqrt{2}} (|1\rangle + e^{i\phi}|2\rangle). \quad (4.1)$$

The relative phase of the two spin states (ϕ), which gives the orientation of the transverse spin

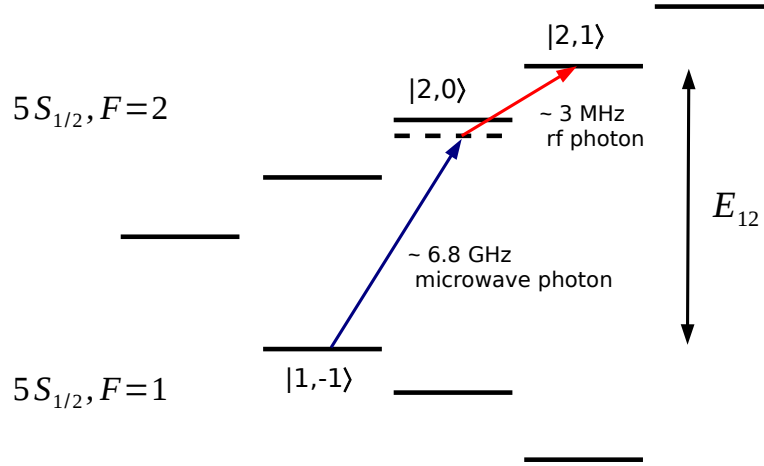


Figure 4.1: Zeeman-shifted ground state hyperfine levels of ^{87}Rb in low magnetic field. The pseudo-spin $\frac{1}{2}$ system consists of the two trapped states ($|1, -1\rangle$ and $|2, 1\rangle$) coupled via a two-photon transition. The coupling fields are detuned from the intermediate $|2, 0\rangle$ state to avoid real transitions.

component in the Bloch representation [27, 28], increases over time in proportion to the energy splitting between the two states E_{12} :

$$\phi = \frac{E_{12}t}{\hbar}. \quad (4.2)$$

By controlling the energy splitting between the two states, or in other words the differential potential experienced by the two spin states ($|1\rangle$ and $|2\rangle$), we control the phase relationship and can initialize the system with desirable spin-state profiles in order to generate different types of spin dynamics, such as spin waves [26, 29] or instabilities.

4.1.1 Differential potential

The trapped atoms in states $|1\rangle$ and $|2\rangle$ experience a differential potential U_{diff} that is a result of two competing mechanisms: the Zeeman shift and a mean-field collisional shift. The Zeeman shift caused by the trapping magnetic field scales with axial position approximately as z^2 (see

Section 4.1.2). The mean-field collisional shift due to interactions between the atoms is given by

$$\Delta_{MF} = \frac{4\pi\hbar^2}{m}[2a_{22}n_2 - 2a_{11}n_1 + 2a_{12}(n_1 - n_2)], \quad (4.3)$$

where m is the mass of a ^{87}Rb atom, a_{ij} is the s-wave scattering length between states $|i\rangle$ and $|j\rangle$ ($i, j=1,2$), and n_i is the density of atoms in state i [26]. This energy shift scales directly with the density; therefore it has a Gaussian profile across the cloud.

By adjusting the magnetic field or the density of the atomic cloud, we can roughly cancel out these two effects to create an approximately uniform differential potential (Fig. 4.2) and then introduce arbitrary differential potentials using external fields. We use the optical field of a laser to alter atomic energy levels via the ac Stark effect in our experiment. This technique allows us to produce differential potentials with adjustable geometry and magnitude.

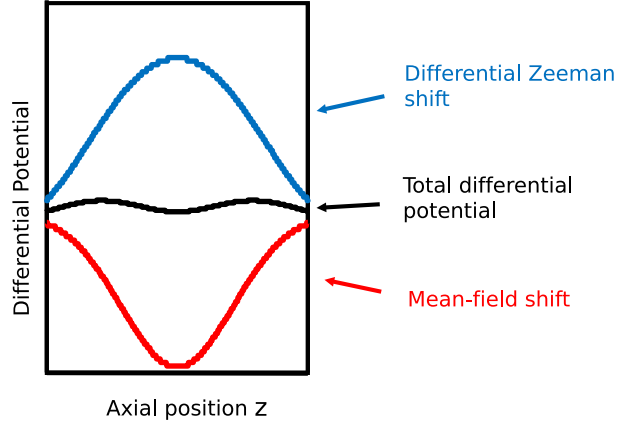


Figure 4.2: Schematic representation of the cancellation of the differential mean-field and Zeeman shifts. The mean-field differential potential is a Gaussian, while the Zeeman shift approximately scales as z^2 . The total differential potential is roughly uniform across the atomic cloud.

4.1.2 Differential Zeeman shift measurement

The presence of an external magnetic field lifts the degeneracy in energy between the states with different m_f values. For the case of $J = \frac{1}{2}$ which applies to the $S_{1/2}$ ground state, the Breit-

Rabi formula gives the dependence of the energy shift of each m_f level, $E(F = I \pm \frac{1}{2}, m_f)$, as a function of magnetic field [30]

$$E(F = I \pm \frac{1}{2}, m_f) = \frac{-\Delta E_{\text{hf}}}{2(2I + 1)} - g_i m_f \mu_B B \pm \frac{\Delta E_{\text{hf}}}{2} \sqrt{1 + \frac{4m_f}{2I + 1} x + x^2}, \quad (4.4)$$

with

$$x = \frac{(g_i + g_j) \mu_B B}{\Delta E_{\text{hf}}}. \quad (4.5)$$

Here ΔE_{hf} is the hyperfine splitting between the two states ($F = 1$ and $F = 2$) at zero magnetic field, I is the nuclear spin ($I = \frac{3}{2}$ for ^{87}Rb), μ_B is the Bohr magneton, g_j is the Landé g -factor and g_i is the nuclear g -factor.

The Breit-Rabi formula predicts a minimum for the transition frequency between the two states ($\nu_{12} = E_{12}/h$) at $B_0 = 3.23$ G, indicating that at $B = B_0$ the differential potential between the two states is first-order independent of the magnetic field. The differential shift near B_0 can be approximated by $\nu_{12} = \nu_{\text{min}} + \alpha (B - B_0)^2$. It is desirable to choose the magnetic field value close to B_0 to reduce the spatial inhomogeneity of ν_{12} across the cloud.

To calibrate the magnetic field we measure ν_{12} as a function of the trapping magnetic field. We adjust the magnetic field by changing the voltage across the bias coils in the HIP trap. This in turn modifies the magnetic field in the center of the trap $B = B_{\text{Pinch}} - aV_{\text{Bias}}$. Then the differential shift is measured by means of Ramsey spectroscopy (see Section 5.1.2). Figure 4.3 effectively shows the measured magnetic field dependence of the transition frequency.

4.1.3 Cancellation of the differential shifts and uniform differential potential

To reach the magnetic field and the density conditions under which the differential potential is uniform, we keep the magnetic field constant and change the collisional energy shift by varying the density of the atomic cloud. We work close to B_0 at a cancellation magnetic field B_C that produces a differential Zeeman shift with a quadratic spatial dependence and an opposite sign to that produced by the collisional shift; otherwise cancellation is not possible. We measure the differential potential experienced by atoms using Ramsey spectroscopy. The uniform differential potential created using this procedure is presented in Fig. 4.4. Adding arbitrary differential potentials to this uniform potential is possible by applying external fields such as a laser field.

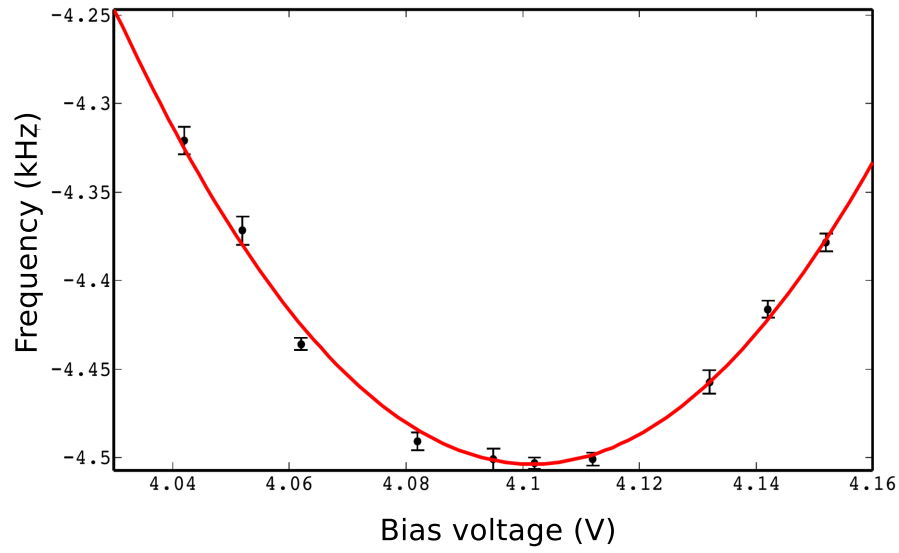


Figure 4.3: Differential Zeeman shift $\frac{1}{h} [E_{12} - E_{\text{hf}}(B = 0)]$, for the $|1, -1\rangle \rightarrow |2, 1\rangle$ transition in low magnetic fields. The red curve is a fit to the quadratic approximation of the Breit-Rabi equation for scale parameter a in $B = B_{\text{Pinch}} - aV_{\text{Bias}}$.

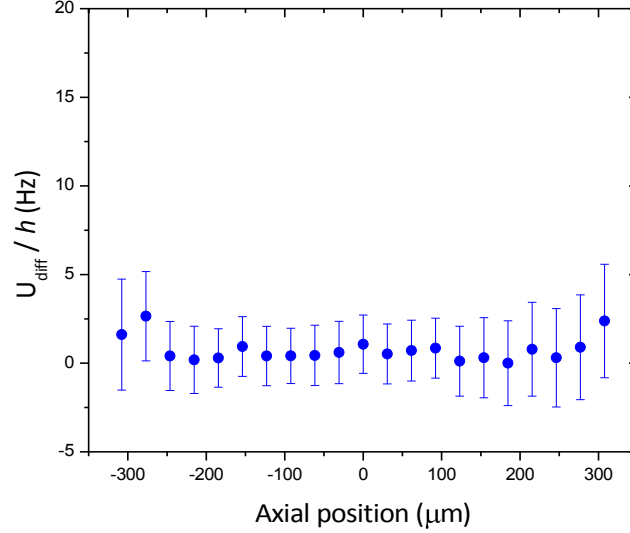


Figure 4.4: Uniform differential potential is achieved by cancellation of the differential Zeeman shift and the collisional mean-field shift. We measure differential energy shifts by means of Ramsey spectroscopy (Section 5.1.2). We obtain spatially resolved data by dividing the atomic cloud axially into 23 bins across the cloud and radially averaging over each bin.

4.1.4 The ac Stark effect and the light shift

The oscillating electromagnetic field of an off-resonant laser alters the atomic energy levels via the ac Stark effect. The electric field of the laser induces an atomic electric dipole moment. According to [31] the resulting interaction potential between this induced dipole moment and the electric field is

$$U_{\text{dip}}(z) = -\frac{3\pi c^2}{2\omega_0^3} \left(\frac{\Gamma}{\omega_0 - \omega_L} + \frac{\Gamma}{\omega_0 + \omega_L} \right) I(z), \quad (4.6)$$

where Γ is the excited state spontaneous decay rate, ω_0 is the transition frequency, ω_L is the applied laser frequency and $I(z)$ is the laser intensity spatial distribution.

When the laser frequency is tuned close to resonance, *i.e.* $|\Delta| = |\omega_L - \omega_0| \ll \omega_0$, implementing the rotating wave approximation leads to a simplified expression for U_{dip} ,

$$U_{\text{dip}}(z) = \frac{3\pi c^2}{2\omega_0^3} \left(\frac{\Gamma}{\Delta} \right) I(z). \quad (4.7)$$

By producing different laser intensity distributions across the atomic cloud, we can create differ-

ential potentials with arbitrary geometries in order to produce spin profiles appropriate to drive different types of spin dynamics.

4.1.4.1 The Stark laser

We use a 180 mW external cavity diode laser with a center wavelength at 780 nm to Stark shift the energy levels. To stabilize the frequency of this laser, we use the PLL lock setup discussed earlier in Section 3.2.2. We detune the laser frequency 3 GHz below the cooling transition by tuning the frequency of the local oscillator (Fig 3.6). This locking procedure gives us the flexibility to adjust the laser detuning. By illuminating the atomic cloud with the laser beam at 3 GHz detuning and 130 W/m^2 intensity, we produce differential light shifts of the order of $\hbar \times 10 \text{ kHz}$. We can modify the magnitude of the differential light shift by either adjusting the intensity of the laser beam or varying the laser detuning.

4.2 Spin-profile initialization

To create and subsequently observe the Castaing instability we need to initialize the atomic cloud with a gradient in its spin profile. We designed two different methods to create these spin gradients; both methods require the same optical setup but then involve different spin initialization sequences.

4.2.1 Optical setup and beam shaping

To create a longitudinal spin gradient we need the atomic cloud to be in a state where spatially half of the cloud is in state $|1\rangle$ and the other half in state $|2\rangle$. We use a step optical potential to produce the spin-profile gradient. We illuminate the atomic cloud with a masked off-resonant laser beam from our Stark laser, as shown schematically in Fig. 4.5. Thereby we shift the energy levels on one side of the cloud and leave the other half of the atomic cloud unperturbed, creating a step optical potential across the atomic cloud. In the next section I will describe how we use this optical potential in preparing the spin profiles.

Figure 4.6 shows the optical setup used to create the step optical potential presented in Fig. 4.7. We use a pair of cylindrical lenses to expand a collimated laser beam axially, mask the expanded beam using a dark blade and finally image the mask onto the atomic cloud by means of a single spherical lens.

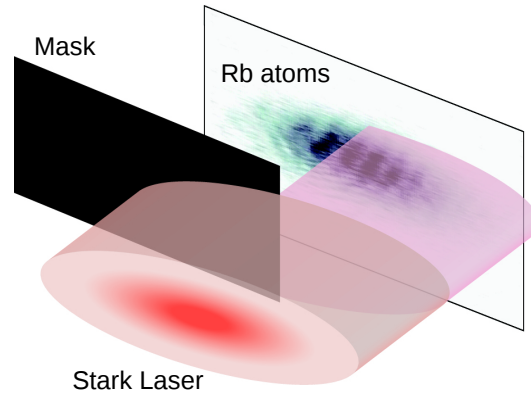


Figure 4.5: A step optical potential is produced by masking the off-resonant laser beam (schematic representation).

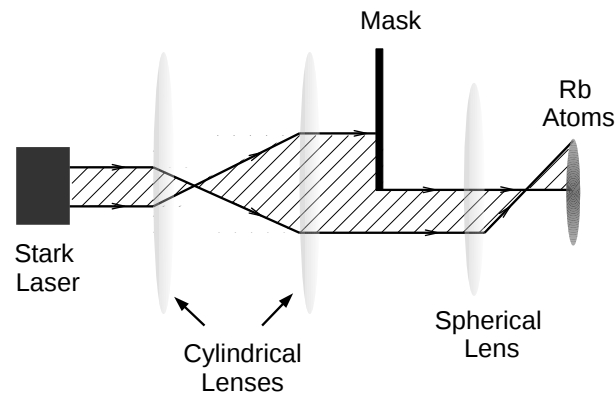


Figure 4.6: Optical setup used in producing the step optical potential presented in Fig. 4.7. The collimated beam from the laser is expanded axially using a pair of cylindrical lenses. The dark mask is imaged on the atomic cloud by a single spherical lens.

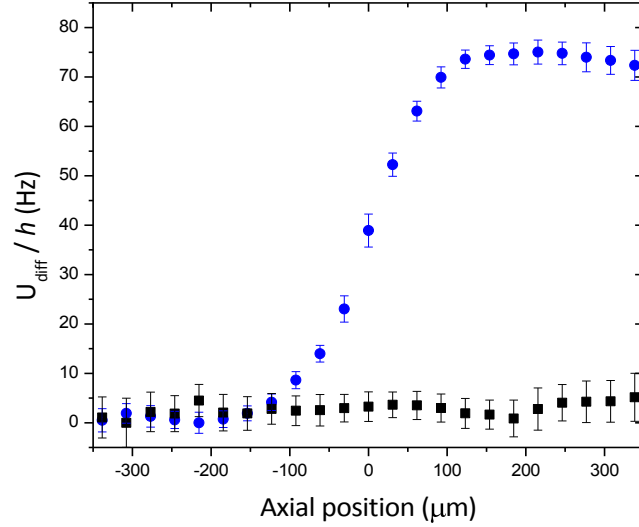


Figure 4.7: Step optical potential (●) with $dU_{\text{diff}}/dz \simeq h \times 500$ Hz/mm created by illuminating the atomic cloud with a masked laser beam. The black data points (■) shows the uniform differential potential with no laser field applied. U_{diff} is measured by means of Ramsey spectroscopy.

4.2.2 Spin-state preparation

At this point we choose between two different approaches to initialize the longitudinal spin profile. If we initialize the atomic cloud in a superposition of the two spin states, subsequent illumination with the masked beam from the Stark laser imprints a phase profile onto the transverse spin component, producing a gradient in the spin profile (∇S_{\perp}). Figure 4.8 shows the experimental sequence used for producing a longitudinal spin gradient in this way. First the atomic cloud is initialized in a coherent superposition of the two spin states by applying a $\pi/2$ pulse. Next the Stark laser is turned on for the phase imprinting time t_{ϕ} , to create a π phase shift between the two sides of the atomic cloud. The second $\pi/2$ pulse then maps the transverse spin into longitudinal spin. As a result of the imprinted phase profile, the second $\pi/2$ pulse transfers the atoms on one side of the atomic cloud into state $|2\rangle$ and the atoms in the other half return to state $|1\rangle$. This procedure leads to a nonequilibrium longitudinal spin gradient across the sample. The phase imprinting happens in a few milliseconds, which is much faster than the trap and spin dynamics.

Figure 4.9a presents typical data showing the initialized longitudinal spin profile across the atomic cloud. We measured the spatial distribution of the numbers N_1 and N_2 of atoms in states

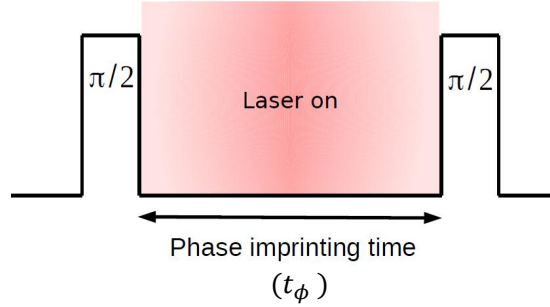


Figure 4.8: The longitudinal spin gradient initialization sequence. Turning on the Stark laser when the system is in a superposition of the states $|1\rangle$ and $|2\rangle$ (*i.e.* after the first $\pi/2$ pulse) imprints a phase profile onto the transverse spin component. A second $\pi/2$ pulse maps the transverse spin into the longitudinal component.

$|1\rangle$ and $|2\rangle$ after applying the spin-initialization sequence (see Section 5.1). The population of the atoms is symmetrically distributed between the two states along the axial extent of the cloud, and thus a gradient in the longitudinal spin component is established. The longitudinal spin presented in Fig. 4.9b is extracted as $S_{\parallel} = \frac{1}{2} (N_2 - N_1) / (N_1 + N_2)$. The maximum linear longitudinal spin gradient implied by these data is $\nabla S_{\parallel} = 1/200 \mu\text{m}^{-1}$. This corresponds to a gradient length scale $l_{\nabla S_{\parallel}} \simeq 1.1 w_z$, where $w_z = 180 \mu\text{m}$ is the Gaussian half-width of the atomic distribution in the axial dimension.

The method described above has several limitations. The most important one is that in the process of creating the longitudinal spin gradient some non-zero transverse spin component is left in the middle of the atomic cloud. This initial transverse spin component makes the signature of the instability less clear as will be discussed in more detail in Section 5.2.2. Also the gradient preparation process is sensitive to the pulse durations and frequencies used to induce the two-photon transition. Any imperfections in the optical potential will also affect the spin gradient initialization.

Using the same phase imprinting method, we can produce transverse spin profiles with sharp gradients to investigate the Castaing instability in the longitudinal spin channel. To create these transverse spin profiles we eliminate the second $\pi/2$ pulse in the sequence presented in Fig. 4.8, *i.e.* we create a transverse spin gradient by illuminating the cloud with the step optical potential but no mapping to the longitudinal spin component is performed. We use these transverse spin gradients

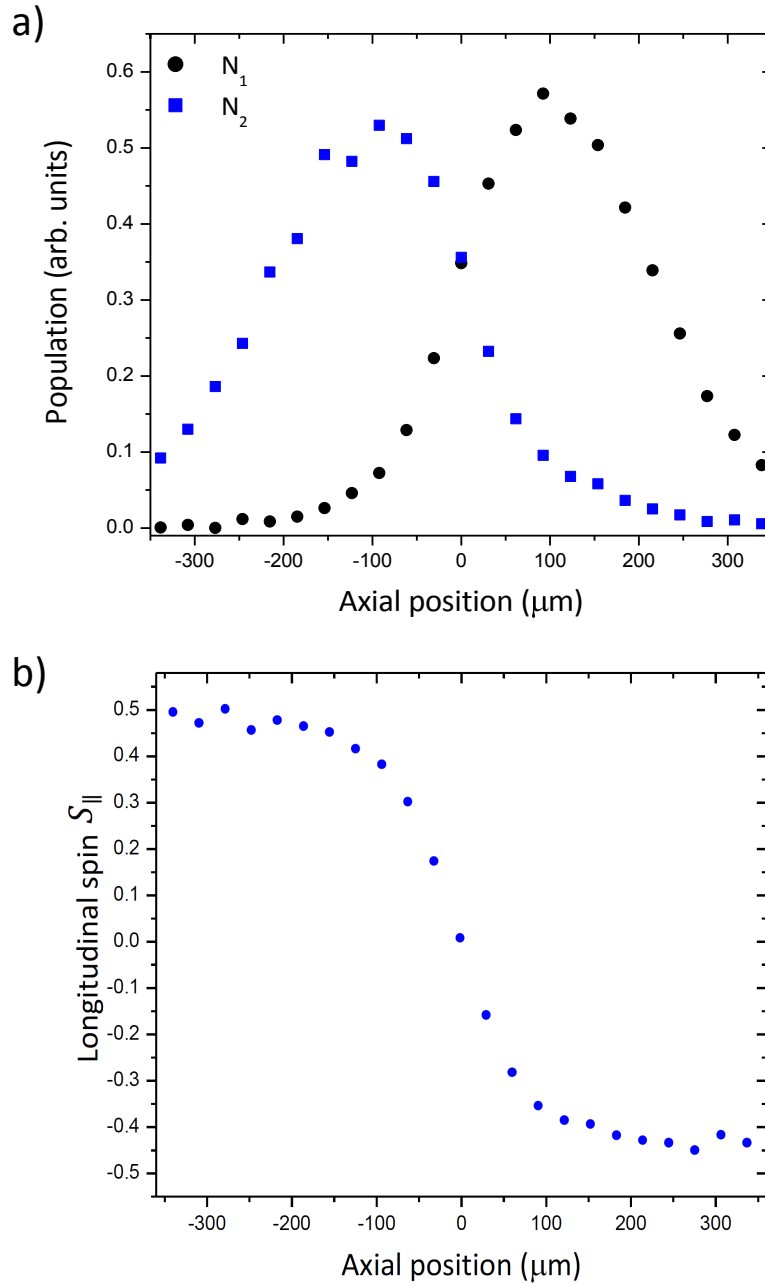


Figure 4.9: (a) Population distribution between states $|1\rangle$ (\bullet) and $|2\rangle$ (\blacksquare) along the axial extent of the atomic cloud, demonstrating the presence of a longitudinal spin gradient. The longitudinal spin profile is obtained by directly measuring the populations N_1 and N_2 of the atoms in the two states immediately after the spin-profile initialization. (b) The longitudinal spin, $S_{\parallel} = \frac{1}{2}(N_2 - N_1)/(N_1 + N_2)$. The gradient length scale implied by this data is $l_{\nabla S_{\parallel}} \simeq 1.1 w_z$, where w_z is the Gaussian half-width of the atomic distribution in the axial dimension.

to study the behavior of the Castaing instability in the longitudinal spin channel.

The second method of initializing a longitudinal spin gradient does not use phase imprinting on the transverse spin component. As discussed earlier, illuminating the sample with the masked laser beam alters the energy levels on one side of the cloud. If this light shift is large compared to the resonant Rabi frequency (3.2 kHz in our experiment), then the atomic energy levels on the bright side of the cloud are shifted enough such that a π pulse resonant with the atoms on the dark (unperturbed) side of the cloud is far detuned for the atoms on the bright side of the atomic cloud, and thus will not transfer the atoms between the two states.

Figure 4.10 illustrates this procedure using the Bloch sphere representation of a two-level system. On the perturbed side (Fig. 4.10a) a state vector initially in the $|1\rangle$ state does not transfer to the $|2\rangle$ state but on the unperturbed side (Fig. 4.10b) the state vector oscillates between the two states.

To implement the second spin gradient initialization procedure we start with the whole sample in the $|1\rangle$ state. Then we apply a π pulse resonant with the unperturbed atoms while the Stark laser is on. This process transfers the atoms on the dark side of the sample to the state $|2\rangle$ while the atoms on the perturbed side remain in the initial state $|1\rangle$, resulting in a longitudinal spin gradient across the cloud. Using this approach we expect to have less transverse spin component left in the middle of the atomic cloud. We are planning to use this method in future experiments.

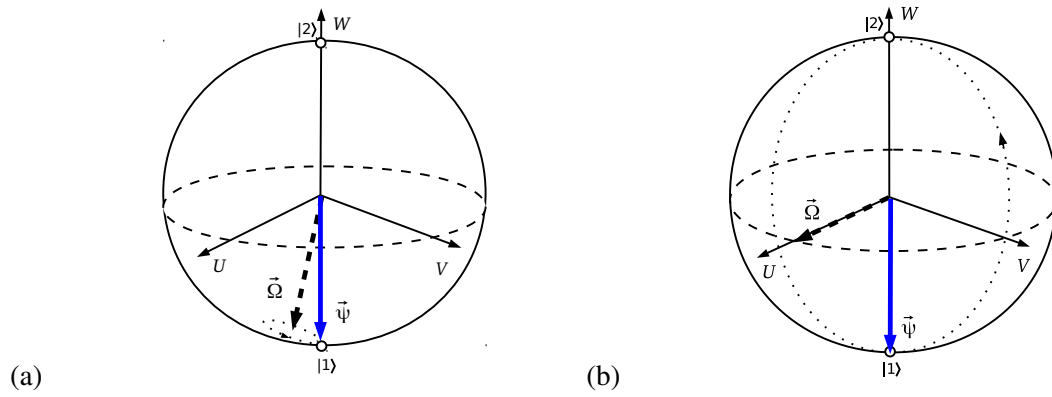


Figure 4.10: (a) The Bloch sphere representation of an atom on the bright (perturbed) side of the sample. The state vector $\vec{\psi}$ (blue arrow) undergoes a small precession around the field's torque vector $\vec{\Omega}$ (dashed arrow) which is far detuned from resonance. (b) The Bloch sphere representation of an atom on the dark (unperturbed) side of the sample. The state vector $\vec{\psi}$ oscillates between the two states, precessing around the field's torque vector $\vec{\Omega}$ which is on resonance.

Chapter 5

Experimental results

The presence of smoothly varying inhomogeneities in the transverse spin component will lead to generation of spin wave oscillations in a spin-polarized system [6, 29]. As discussed in Chapter 2, introducing sufficiently sharp gradients in the spin profile alters the spin dynamics dramatically, resulting in the generation of instabilities. In this chapter I will describe the experimental method used to extract the spin components, or in other words reconstruct the Bloch vector evolution in time. Finally, I will present the experimental results extracted using this method, manifesting evidence for the presence of the Castaing instability.

To investigate the Castaing instability we first initialize a spin profile containing a gradient, as described in Section 4.2.2. We then allow the system to evolve for some period of time, and finally the atomic cloud is imaged in order to measure the transverse and longitudinal spin components as a function of space and time. To achieve spatially resolved measurements we divide the image of the atomic cloud into 23 equally sized axial bins and average radially over each bin. These measurement methods will be discussed in the following section.

5.1 The experimental method for reconstructing spin

We use two different methods to measure the transverse and longitudinal spin components. These methods are described in the following sections.

5.1.1 Longitudinal spin

The longitudinal spin component is extracted from image data by directly measuring the population of atoms N_1 and N_2 in the two states, $|1\rangle$ and $|2\rangle$, subsequent to the evolution of the system. The population in each state is measured in separate experimental shots with the same initial conditions. Typical longitudinal spin distribution data are presented in Fig. 5.1. The longitudinal spin component is determined from N_1 and N_2 using

$$S_{\parallel} = \frac{1}{2} (N_2 - N_1) / (N_1 + N_2). \quad (5.1)$$

The population difference $N_2 - N_1$ is normalized to the total population in each bin $N_1 + N_2$ in order to obtain the longitudinal spin component.

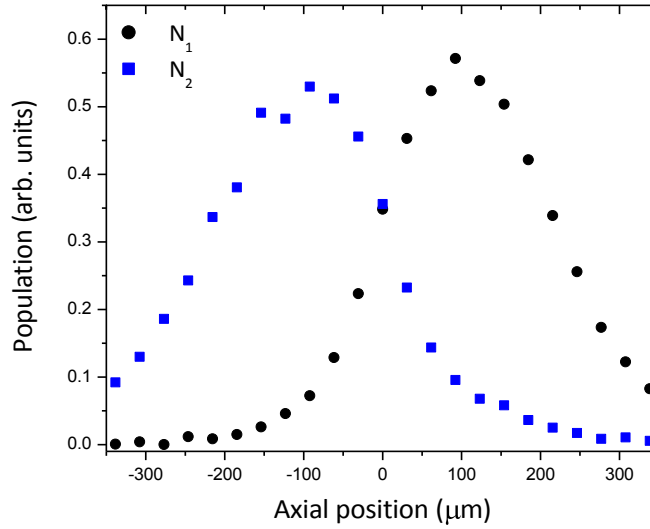


Figure 5.1: Population of atoms in the two states, $|1\rangle$ (●) and $|2\rangle$ (■). The population in each state is measured in separate experimental shots. As described earlier the cloud is divided axially into 23 bins for spatial resolution; here each data point corresponds to one bin. These data are used to reconstruct the longitudinal spin component.

5.1.2 Transverse spin

We use the Ramsey spectroscopy method to reconstruct the transverse spin component. The amplitude of the Ramsey fringes gives the transverse spin amplitude (coherence), and the phase of these

oscillations gives the transverse spin orientation relative to the initial orientation.

5.1.2.1 Ramsey spectroscopy

The Ramsey method consists of two $\pi/2$ microwave pulses detuned from the two-photon transition by $\delta = \omega - \omega_0$ and separated by a varying free evolution time T as indicated in Fig. 5.2. The probability of finding the atoms in the excited state P_2 after the two-pulse sequence for $\delta \ll \Omega_R$ and pulse length $\tau \ll T$ is [26]

$$P_2(T, \delta) = \frac{1}{2} + \frac{1}{2} \cos(\delta T). \quad (5.2)$$

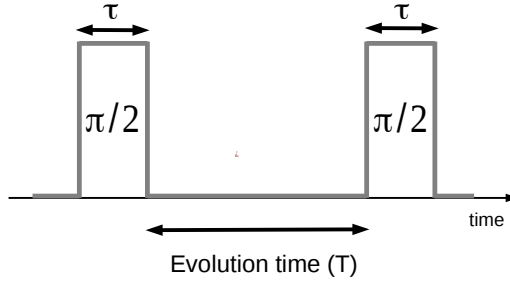


Figure 5.2: Ramsey spectroscopy sequence.

The first $\pi/2$ pulse places the atoms in a coherent superposition of the two spin states. During the evolution time, the relative phase between the two states evolves proportional to the energy difference between them (Eq. 4.2). The second $\pi/2$ pulse recombines the two states interferometrically, depending on their relative phase. As a result, an oscillation of the population between the two states is observed as a function of the evolution time. Figure 5.3 illustrates this process schematically in the Bloch sphere representation. This first $\pi/2$ pulse applied in the spin gradient initialization sequence in Fig. 4.8 is the reference pulse (the first $\pi/2$ pulse) in Ramsey spectroscopy sequence.

Typical Ramsey spectroscopy experimental data are presented in Fig. 5.4. The frequency of Ramsey oscillations depends only on the detuning from resonance and characterizes the energy

splitting of the two states. Measuring the number of atoms in state $|1\rangle$ after the second $\pi/2$ pulse is equivalent to measuring the transverse spin (S_\perp) before the second $\pi/2$ pulse is applied. Thus the amplitude of the Ramsey fringes gives the transverse spin magnitude.

5.2 Results

5.2.1 Castaing instability with a longitudinal spin gradient

The first observations of the Castaing instability during the 1990s, as was initially predicted by B. Castaing in 1984 [19], were made in connection with longitudinally spin-polarized liquid ^3He - ^4He samples in which a gradient in the spin profile had been imprinted [27, 32, 33]. According to theoretical predictions a purely longitudinal spin profile with a sharp gradient leads to spontaneous generation of transverse spin waves in the presence of a small transverse perturbation. The initial longitudinal spin gradient in these spin-polarized systems was produced by applying a π pulse on one side of the sample, and the resulting instability led to NMR ringing on free induction decay [27, 32, 33].

Despite the fact that trapped atomic samples of Alkali-metal gases are different than condensed spin-polarized liquids insofar as a number of experimental parameters are concerned (*e.g.* smaller sizes and nonuniform density distributions) numerical simulations performed by J. N. Fuchs *et al.* [18] confirmed that observation of the Castaing instability ought to be feasible in such systems (see Chapter 2). In this work we present the results of the first experimental investigation of the Castaing instability in a trapped ^{87}Rb gas.

To study the instability in the transverse spin channel we first initialize a longitudinal spin gradient as illustrated in Fig. 4.9b, using the first method described in Section 4.2.2. Following the spin-state preparation, the atomic cloud is allowed to evolve and is then imaged to extract the spin components, using the methods outlined in Section 5.1. According to the theoretical studies summarized in Chapter 2, a rise in the magnitude of the transverse spin component at the initial stage of the evolution of dynamics is the signature for the Castaing instability. Theoretical estimates of the time required for the development of the instability with our experimental parameters is $t_{\text{inst}} \sim 200$ ms [18]. This rise in the transverse spin magnitude is the sign we expect to see in the experimental data.

Figure 5.5 shows Ramsey oscillation data measured up to $T = 350$ ms for a bin at $z = 250$ μm from the center of the atomic cloud. It is clearly seen that the initial Ramsey fringe amplitude is

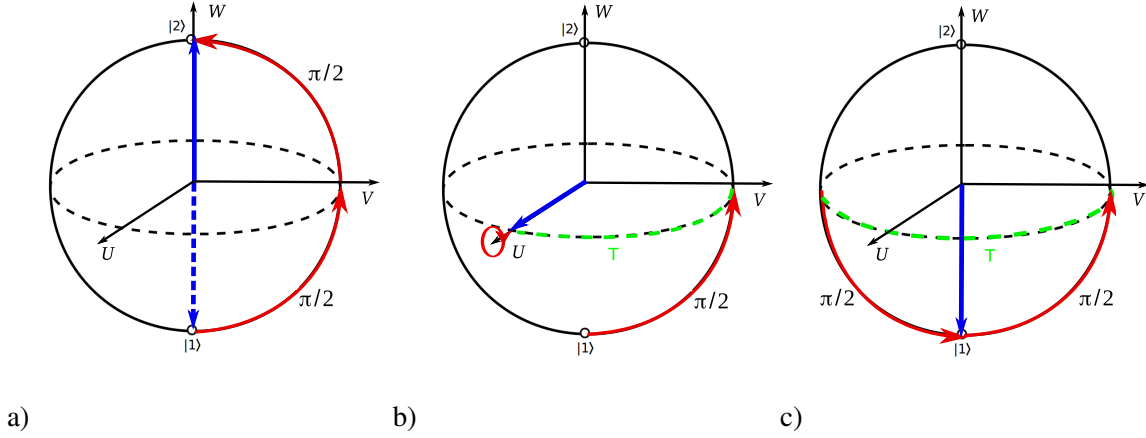


Figure 5.3: Schematic representation of Ramsey oscillations in the Bloch sphere representation, showing two $\pi/2$ pulses detuned by $\delta = \omega - \omega_0$ and separated by an evolution time T . The blue dashed arrow indicates the initial state. (a) When $\delta T = 0$ the two-pulse sequence is equivalent to a π pulse. (b) When $\delta T = \frac{\pi}{2}$ the second $\pi/2$ pulse does not transfer the atoms into state $|2\rangle$ as the state vector is along the field's torque vector (U -axis). (c) When $\delta T = \pi$ the second $\pi/2$ transfers the atoms back into the initial state $|1\rangle$.

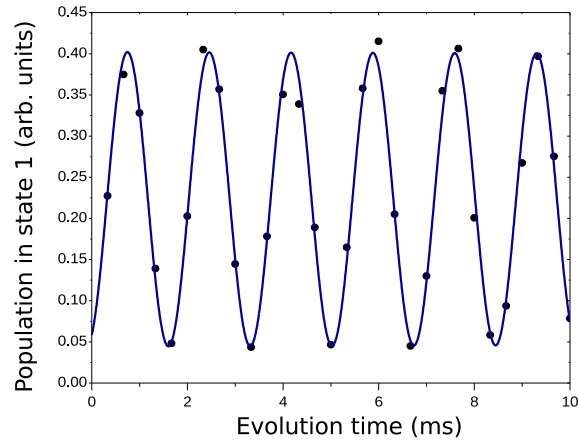


Figure 5.4: Typical Ramsey oscillation data. The curve represents a sine wave fit to the data.

small, indicating that the initial transverse spin component is also small. But at around $T = 50$ ms a rapid rise in the magnitude of the transverse spin is observed. The behavior observed in the center of the atomic cloud is different. A large initial transverse spin component is present (Fig. 5.6). This large initial spin component in the middle of the cloud is due to our spin-state initialization technique, and makes the signature of the instability less clear.

To extract the time evolution of the magnitude and phase of the transverse spin, we fit a sine wave with a fixed frequency but a time varying amplitude and phase to Ramsey oscillations. As illustrated in Fig 5.7 to do this we choose a window with a size larger than one oscillation. For example, the running window used for extracting the data presented in Fig. 5.8 encompasses 15 data points, *i.e.* the window size is 50 ms. We extract the amplitude and phase of the oscillations in this window. This window is moved in time through the data set to extract the time evolution of the amplitude and phase.

Data characterizing the magnitude of the transverse spin component extracted from the Ramsey oscillation raw data is summarized in Fig. 5.8, showing the evolution of the transverse spin magnitude (the Ramsey fringe amplitude) as a function of time. The red and black curves show the behavior observed at the center and edge of the sample, respectively. The edge of the atomic cloud is initially in a nearly pure longitudinal spin state (small transverse spin component), but after a short time a rapid rise in the magnitude of the transverse spin is observed (also see Fig. 5.5). In the center of the cloud the transverse spin magnitude decreases gradually without showing any evidence for anomalous behavior.

The time evolution of the transverse spin phase extracted from different Ramsey oscillation data is presented in Fig. 5.9. The system initially starts with a gradient in the transverse spin phase across the cloud. This situation is then stable (no observable dynamics) for hundreds of milliseconds. At $T = 280$ ms a sudden inversion in the orientation of the transverse spin is observed. Longitudinal spin evolution measurement show that this time scale is coincident with the inversion time of the longitudinal spin gradient. This time scale is different from the trap frequency; therefore this inversion is due to the dynamics occurring associated with the spin degree of freedom in the system. The observed dynamics get damped by elastic collisions between the atoms that randomize the spin. Also dipolar relaxation that leads to loss from the $|2\rangle$ state causes longitudinal relaxation. The damping time for the dynamics is of the order of 400 ms, and therefore no further inversions could be observed in these experiments.

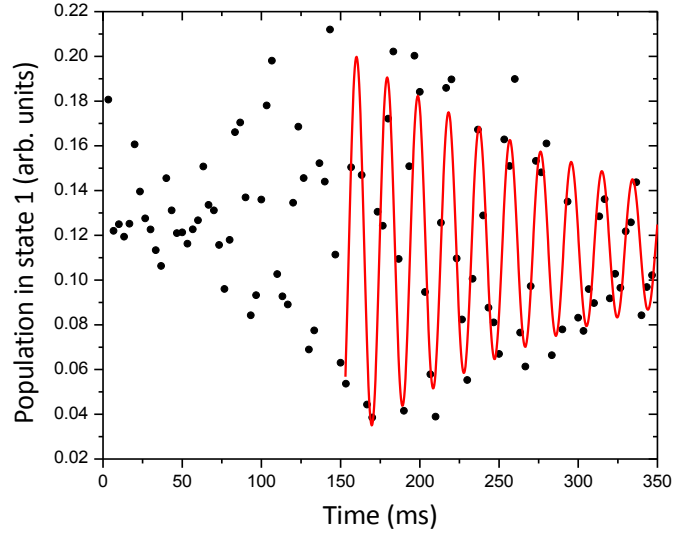


Figure 5.5: Ramsey oscillations for a bin at $z = 250 \mu\text{m}$ from the center of the atomic cloud. The initial fringe amplitude is small, but is followed by a rapid rise. The solid line represents a fit to a damped sine wave to guide the eye.

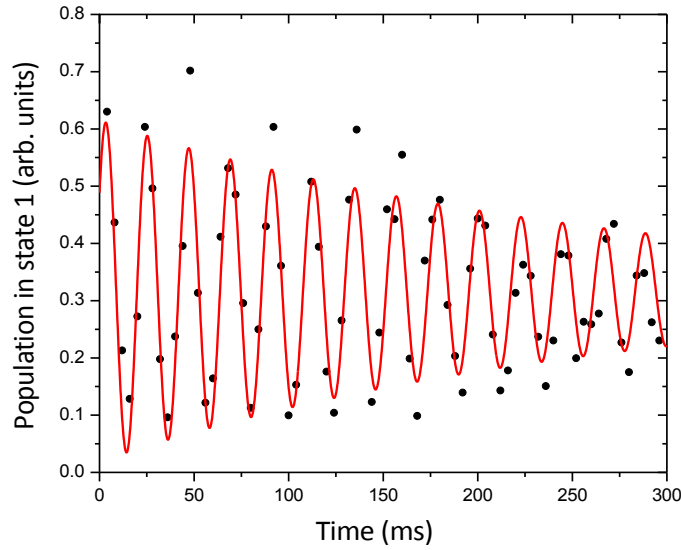


Figure 5.6: Ramsey oscillations in the middle of the atomic cloud. There is a large initial transverse spin component due to the spin-state preparation technique. The solid line represents a fit to a damped sine wave to guide the eye.

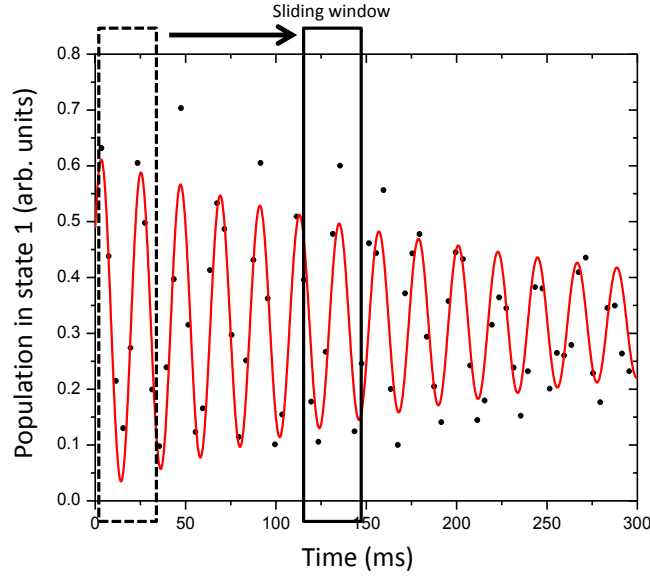


Figure 5.7: A sine wave with a fixed frequency but a time varying amplitude and phase is fit to the data points in a window with a width that encompasses more than one oscillation. This window is moved in time through the data set to extract the time evolution of the amplitude and phase of the Ramsey oscillations. The solid line is a fit of a damped sine wave to guide the eye.

5.2.2 Castaing instability with a transverse spin gradient

As was discussed in Chapter 2 and as previously observed in [6, 29], spin waves are excited in systems with smoothly varying inhomogeneities in their transverse spin profile. To investigate how the presence of the Castaing instability alters spin dynamics in such systems, we also studied an atomic cloud initialized with a gradient in its transverse spin profile. In order to imprint a transverse spin gradient, we first initialize the system in a coherent superposition of states $|1\rangle$ and $|2\rangle$ by applying a $\pi/2$ pulse to a system initially in the $|1\rangle$ state. The atomic cloud is then illuminated by the masked off-resonant laser, imprinting a sharp gradient in the transverse spin profile (see Section 4.2.2). Following the spin-profile preparation we allow the system to evolve in time and finally measure the transverse spin component using Ramsey spectroscopy.

Figure 5.10 shows Ramsey oscillations measured up to $T = 300$ ms for (a) a bin in the center and (b) a bin at $z = 250 \mu\text{m}$ from the center of the atomic cloud. In the center of the cloud we observe the Ramsey oscillations damping gradually due to elastic collisions (Fig. 5.10a). On the contrary, on the edge of the cloud at around $T = 180$ ms (Fig. 5.10b) a collapse in coherence is observed similar to the collapse and revival of coherence observed in [34].

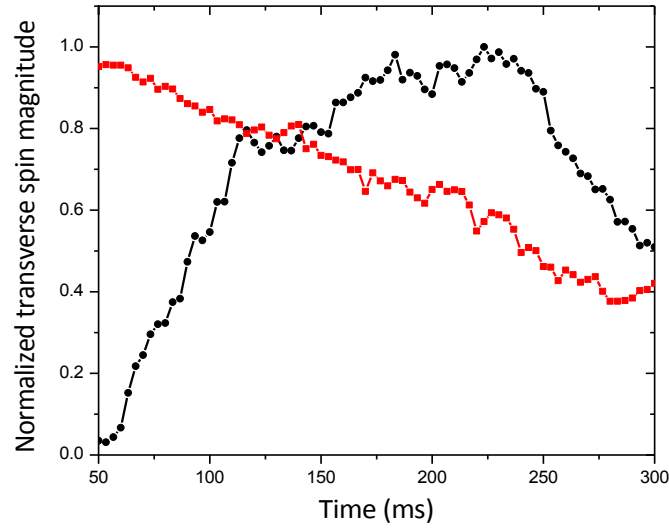


Figure 5.8: Time evolution of the magnitude of the transverse spin in a cloud initialized with a longitudinal spin gradient. These results are extracted from raw Ramsey oscillation data by fitting a sine wave with a time varying amplitude and phase to Ramsey oscillations. The extracted amplitude of the Ramsey oscillations is normalized with the mean value of the Ramsey oscillations in each bin. The black curve (\bullet) indicates data acquired at $z = 250 \mu\text{m}$ from the center of the atomic cloud (Fig. 5.5) where the initial condition corresponds to a nearly pure longitudinal spin state with a small initial transverse spin component. After a short delay a rapid rise in the magnitude of the transverse spin is observed. The red curve (\blacksquare) corresponds to the center of the cloud where a large initial transverse spin component is present.

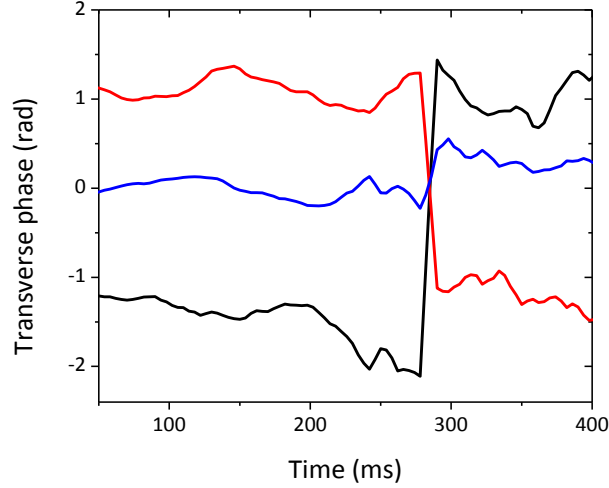


Figure 5.9: Time evolution of the transverse spin phase in a system initialized with a longitudinal spin gradient. The red, blue and black curves show the right, middle and left sides of the sample respectively. At $T = 280$ ms a sudden inversion in the orientation of the transverse spin is observed on the edges of the cloud.

The collapse in the coherence is associated with collisions between atoms with significantly different phase, such that the identical spin rotation effect (see Section 2.2.2) cannot rephase the spins into a uniform distribution. The spin profile we imprint on the transverse spin produces regions with dramatically different phases residing close to each other, since the phase on the two sides of the cloud differ by π . The motion of the atoms in the confining potential can lead to collisions between atoms from the two different sides of the cloud. These collisions lead to a collapse in the coherence observed at those regions in the cloud. Due to the gradient in the center of the cloud the neighboring atoms in the middle have only slightly different spin orientations; therefore no dramatic change in behavior is expected to be observed.

Figure 5.11 shows the evolution of the transverse spin orientation (phase) as a function of time at different parts of the atomic cloud. The red, blue and black curves show the right, middle and left sides of the sample respectively. The system starts with a π difference in the transverse spin orientation across the cloud. It stays in its initial configuration for 150 ms without any observable dynamics, and at around $T = 180$ ms the orientation of the transverse spin is suddenly inverted by π . This behavior is quite different than the slow sinusoidal evolution that is observed for an

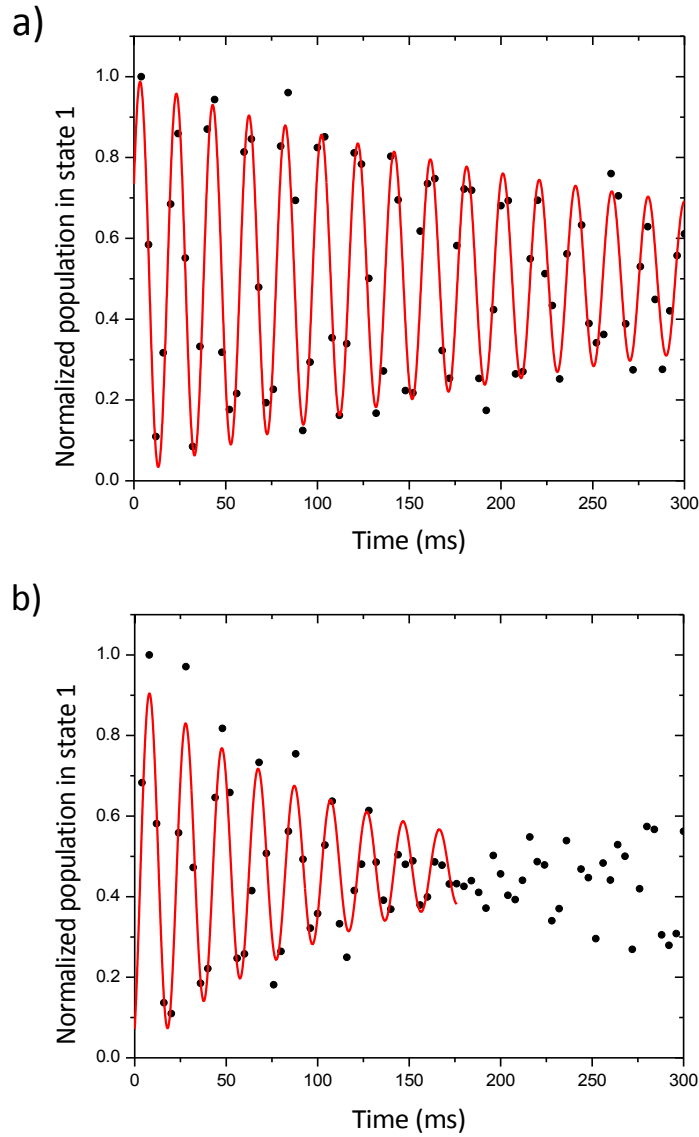


Figure 5.10: Ramsey spectroscopy data (a) in the middle and (b) at $z = 250 \mu\text{m}$ from the center of the atomic cloud, for a system initialized with a gradient in the transverse spin profile. A damped sine wave is fit to the experimental data points to guide the eye. The phase is then measured using the running-window fit described in Section 5.2.1.

ordinary spin wave oscillation mode. This abrupt inversion behavior observed in our experiment distinguishes these effects from normal spin wave oscillation modes.

To quantify the effect we have observed we studied the variation of the spin inversion rate as a function of the magnitude of the spin imprinted at the initialization stage. The time defined as the spin inversion time is indicated on the plot in Fig 5.11 with a dashed line. This inversion time corresponds to the time when the initial spin orientation angle passes through zero as it inverts to an opposite value. The inverse of this quantity is taken as the spin inversion rate. We modify the magnitude of the phase difference by changing the magnitude of the light shift via adjusting the intensity of the applied laser.

We compare the experimental results with the predictions of a numerical solution to the spin transport equation (Eq. 2.6). Figure 5.12 presents the experimental data along with the simulation results. The black curve shows the numerical simulation of the quantum Boltzmann equation for an initial transverse spin profile with a gradient distributed in the middle of the cloud with a length scale of the order of w_z . The red curve shows the simulation results for a linear differential potential of the same magnitude but no sharp gradient. From the simulation results, the presence of the instability leads to dramatically increased spin inversion rates, and the experimental results (blue dots on the plot) agree reasonably with the simulation.

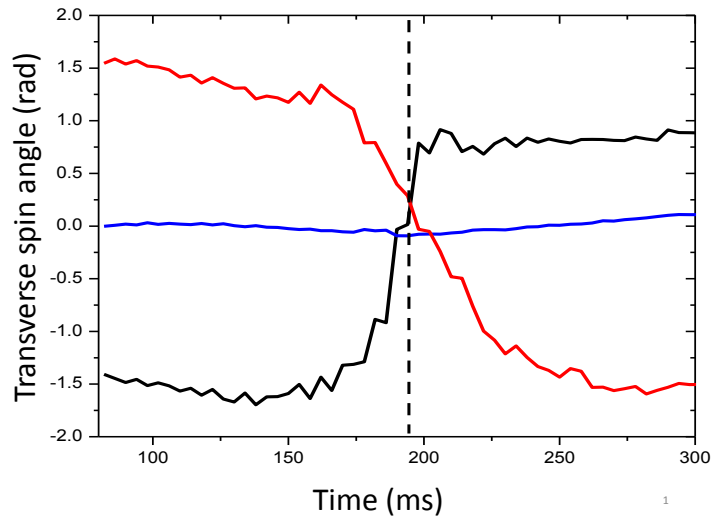


Figure 5.11: Time evolution of the transverse spin phase in a cloud initialized with a sharp gradient in the transverse spin profile measured using the running-window fit described in Section 5.2.1. The red, blue and black curves show the right, middle and left sides of the sample respectively. Initially there is a π difference in the transverse spin phase across the cloud. Very little happens for the first 150 ms followed by a sudden inversion of the transverse spin phase on opposite sides of the cloud. The time defined as the spin inversion time is indicated on the plot with a dashed line. This inversion time corresponds to the time when the initial spin orientation angle passes through zero as it inverts to an opposite value. The spin inversion rate inferred from these data is 5.5 ± 0.3 Hz.

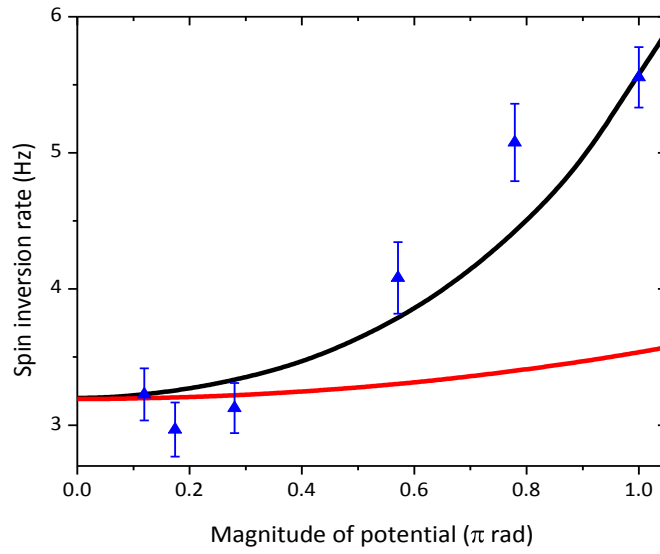


Figure 5.12: Experimental results along with numerical solution of the spin transport equation showing the spin inversion rate as a function of the magnitude of the initial spin difference. The black curve shows the simulation results for an initial transverse spin profile containing a sharp gradient with a length scale on the order of w_z . The red curve shows the solution for similar initial conditions with a linear differential potential of the same magnitude but no sharp gradient. It is evident that the presence of the gradient leads to increased spin inversion rates. The experimental results agree with the simulation results.

Chapter 6

Conclusion

In this thesis I have presented a study of spin dynamics instabilities in a nondegenerate gaseous trapped ^{87}Rb sample. This work represents the first experimental investigation of the so-called Castaing instability in an ultracold atomic quantum gas. The experimental results I have presented manifest the signature for the presence of the Castaing instability.

The Castaing instability is an instability in the spin dynamics of spin-polarized systems, which is associated with the presence of sharp gradients in the spin profile. This instability was initially predicted by B. Castaing in his studies of ^3He samples in 1984 [19]. It was observed in experiments on samples of spin-polarized ^3He - ^4He mixtures [27, 32, 33]. Following the observations of spin dynamics in trapped atomic ^{87}Rb gas in 2002, theoretical and numerical studies carried out by A. Kuklov *et al.* and J. N. Fuchs *et al.* proposed that this instability ought to be observed in such systems. The advantages ultracold atomic systems provide, specifically the possibility of localized imaging, help to study the localized behavior of the instability.

In this work we studied the Castaing instability in a cloud of nondegenerate trapped ^{87}Rb with 7×10^6 atoms (peak density $n = 8.6 \times 10^{19} \text{ m}^{-3}$) at typical temperatures $T \simeq 600 \text{ nK}$ ($T \simeq 1.1 T_c$). The Castaing instability was observed and studied with two different initial spin profiles. In one case the initial spin profile is a purely transverse spin profile containing a sharp gradient ∇S_\perp across the atomic cloud. In the other case the initial spin profile is purely longitudinal with a spin gradient ∇S_\parallel across the atomic cloud.

Imprinting a sharp spin gradient in the transverse spin profile alters the spin dynamics because of the presence of the Castaing instability in the longitudinal spin channel. The experimental results manifest altered dynamics in the form of an abrupt change in behavior of the time evolution of the

spin vector as well as increased spin inversion rates compared to normal modes of spin wave oscillations. The results observed during my experiments are in reasonable agreement with expectations from theoretical studies and with numerical solutions to the spin transport equation we performed.

The Castaing instability experiment in the transverse channel was performed with a longitudinal spin gradient created using the first spin-preparation method discussed in Chapter 4, which involves phase imprinting a transverse spin gradient and then mapping the transverse spin into longitudinal spin using microwave pulse techniques. The experimental results show a rise in the magnitude of the transverse spin component, which is the anticipated signature of the Castaing instability. However, the presence of an initial large transverse spin component in the middle of the atomic cloud makes the signature of the Castaing instability less clear. This initial transverse spin component is present because of the spin-state preparation technique we applied.

We contemplated using other preparation techniques to eliminate this initial transverse component in the middle of the cloud. One of such techniques is the second spin-state preparation method discussed in Chapter 4, which involves using large Stark shifts on one side of the atomic cloud to control the transfer of the atoms between the two spin states. Due to time constraints and issues associated with equipment failure we could not test any alternative methods.

Further evidence that the effects we observed are indeed a result of the Castaing instability lie in the observed time scales. The timescales of the observed dynamics in this work are different from the time scales associated with trap oscillations, thus we can conclude that the dynamics are happening due to the spin degree of freedom. Also the spin oscillations manifest abrupt behavior, which distinguishes these effects from normal modes of spin wave oscillations. However, more investigation is needed to confirm all of the theoretical predictions for the Castaing instability.

Future avenues of inquiry include using alternative spin-state preparation methods to clean up the longitudinal spin gradient through elimination of the transverse spin component in the middle of the atomic cloud. One could also envision imprinting other types of spin profiles on the trapped gas and observing the subsequent dynamics. Another experiment could include studying the dynamics in the presence of such spin profiles in a Bose-Einstein condensate rather than a nondegenerate sample.

Bibliography

- [1] M. H. Anderson, J. R. Ensher, M. R. Matthews, C. E. Wieman, and E. A. Cornell. Observation of Bose-Einstein Condensation in a Dilute Atomic Vapor. *Science*, 269(5221):198–201, 1995.
- [2] M.-O. Mewes, M. R. Andrews, N. J. Van Druten, D. M. Kurn, D. S. Durfee, and W. Ketterle. Bose-Einstein Condensation in a Tightly Confining dc Magnetic Trap. *Physical Review Letters*, 77(3):416–419, 1996.
- [3] Y. Liu, S. Jung, S. E. Maxwell, L. D. Turner, E. Tiesinga, and P. D. Lett. Quantum Phase Transitions and Continuous Observation of Spinor Dynamics in an Antiferromagnetic Condensate. *Physical Review Letters*, 102(12):125301, 2009.
- [4] D. Jaksch. Optical lattices, ultracold atoms and quantum information processing. *Contemporary Physics*, 45(5):367–381, 2004.
- [5] Artur Widera, Olaf Mandel, Markus Greiner, Susanne Kreim, Theodor W. Hänsch, and Immanuel Bloch. Entanglement Interferometry for Precision Measurement of Atomic Scattering Properties. *Physical Review Letters*, 92:160406, 2004.
- [6] H. J. Lewandowski, D. M. Harber, D. L. Whitaker, and E. A. Cornell. Observation of Anomalous Spin-State Segregation in a Trapped Ultracold Vapor. *Physical Review Letters*, 88(7):70403, 2002.
- [7] C. Lhuillier and F. Laloë. Transport properties in a spin polarized gas, I. *Journal de Physique*, 43(2):197–224, 1982.
- [8] J. N. Fuchs, D. M. Gangardt, and F. Laloë. Internal State Conversion in Ultracold Gases. *Physical Review Letters*, 88:230404, 2002.
- [9] T. Nikuni, J. E. Williams, and C. W. Clark. Linear spin waves in a trapped Bose gas. *Physical Review A*, 66(4):043411, 2002.
- [10] M. Ö. Oktel and L. S. Levitov. Internal Waves and Synchronized Precession in a Cold Vapor. *Physical Review Letters*, 88(23):230403, 2002.
- [11] J. E. Williams, T. Nikuni, and Charles W. Clark. Longitudinal Spin Waves in a Dilute Bose Gas. *Physical Review Letters*, 88:230405, 2002.
- [12] A. E. Meyerovich. Quantum and nonlocal coherent effects in Boltzmann gases. *Physical Review B*, 39(13):9318, 1989.

- [13] A. Kuklov and A. E. Meyerovich. Precessing domains and the Castaing instability in confined alkali-metal gases. *Physical Review A*, 66(2):023607, 2002.
- [14] H. J. Metcalf and P. Van der Straten. *Laser Cooling and Trapping*. Springer Verlag, 1999.
- [15] L. Allen and J. H. Eberly. *Optical Resonance and Two-level Atoms*. Dover Publications, 1987.
- [16] J. F. Annett. *Superconductivity, Superfluids, and Condensates*, volume 67. Oxford University Press, 2004.
- [17] A. J. Leggett and M. J. Rice. Spin Echoes in Liquid He^3 and Mixtures: A Predicted New Effect. *Physical Review Letters*, 20:586–589, 1968.
- [18] J. N. Fuchs, O. Prévoté, and D. M. Gangardt. Castaing’s instability in a trapped ultra-cold gas. *The European Physical Journal D-Atomic, Molecular, Optical and Plasma Physics*, 25(2):167–171, 2003.
- [19] B. Castaing. Polarized ^3He . *Physica B+C*, 126:212–216, 1984.
- [20] H. J. Lewandowski, D. M. Harber, D. L. Whitaker, and E. A. Cornell. Simplified System for Creating a Bose-Einstein Condensate. *Journal of Low Temperature Physics*, 132(5):309–367, 2003.
- [21] D. A. Steck. Rubidium 87 D Line Data, available online at <http://steck.us/alkalidata>(revision 2.1.4), 23 December 2010.
- [22] K. B. MacAdam, A. Steinbach, and C. Wieman. A narrow-band tunable diode laser system with grating feedback, and a saturated absorption spectrometer for Cs and Rb. *American Journal of Physics*, 60:1098–1098, 1992.
- [23] R. Thomas. *Characterization of an Apparatus for the Creation of a Bose-Einstein Condensate in Rubidium Vapour*. Bachelor’s thesis, Simon Fraser University, 2010.
- [24] T. Bergeman, G. Erez, and H. J. Metcalf. Magnetostatic trapping fields for neutral atoms. *Physical Review A*, 35(4):1535, 1987.
- [25] W. Ketterle, D. S. Durfee, and D. M. Stamper-Kurn. *Making, probing and understanding Bose-Einstein condensates*, *Proc. Int. School of Physics-Enrico Fermi*. Ed. M. Inguscio et al., Amsterdam: IOS Press, 1999.
- [26] H. J. Lewandowski. *Coherences and correlations in an ultracold Bose gas*. PhD thesis, University of Colorado, 2002.
- [27] Hikota Akimoto, Osamu Ishikawa, Gong-Hun Oh, Masahito Nakagawa, Tohru Hata, and Takao Kodama. Nonlinear effects on spin waves in ^3He - ^4He dilute solutions. *Journal of Low Temperature Physics*, 82(5):295–316, 1991.
- [28] R. P. Feynman, F. L. Vernon, and R. W. Hellwarth. Geometrical Representation of the Schrödinger Equation for Solving Maser Problems. *Journal of Applied Physics*, 28(1):49–52, 1957.

- [29] J. M. McGuirk and L. F. Zajiczek. Optical excitation of nonlinear spin waves. *New Journal of Physics*, 12(10):103020, 2010.
- [30] S. Svanberg. *Atomic and Molecular Spectroscopy: Basic Aspects and Practical Applications*. Springer Verlag, 2004.
- [31] R. Grimm, M. Weidemüller, and Y. B. Ovchinnikov. *Optical Dipole Traps for Neutral Atoms. Advances in Atomic, Molecular, and Optical Physics*, volume 42. Elsevier, 2000.
- [32] R. König, J. H. Ager, R. M. Bowley, J. R. Owers-Bradley, and A. E. Meyerovich. Spin-Wave instabilities in ^3He - ^4He solutions at high magnetic field. *Journal of Low Temperature Physics*, 101(3):833–838, 1995.
- [33] G. Nunes, C. Jin, D. L. Hawthorne, A. M. Putnam, and D. M. Lee. Spin-polarized 3 – ^4He solutions: Longitudinal spin diffusion and nonlinear spin dynamics. *Physical Review B*, 46:9082–9103, 1992.
- [34] J. M. McGuirk and L. F. Zajiczek. Localized collapse and revival of coherence in an ultracold Bose gas. *Physical Review A*, 83(1):013625, 2011.